PNAS

Main Manuscript for

A redox switch allows binding of Fe(II) and Fe(III) ions in the cyanobacterial iron binding protein FutA from *Prochlorococcus*

Rachel Bolton[a,b], Moritz M. Machelett[a,c], Jack Stubbs[a,b], Danny Axford[b], Nicolas Caramello[d,e], Lucrezia Catapano[f,g], Martin Malý[a], Matthew J. Rodrigues[a,b,h], Charlotte Cordery[a,b], Graham J. Tizzard[i], Fraser MacMillan[j], Sylvain Engilberge[d,k], David von Stetten[l], Takehiko Tosha[m], Hiroshi Sugimoto[m], Jonathan A.R. Worrall[n], Jeremy S. Webb[a,o], Mike Zubkov[c,p], Simon Coles[i], Eric Mathieu[k], Roberto A. Steiner[f,q], Garib Murshudov[g], Tobias E. Schrader[r], Allen M. Orville[b,s], Antoine Royant[d,k], Gwyndaf Evans[b,t], Michael A. Hough[b,n,s], Robin L. Owen[b], Ivo Tews[a,1]

[a] Biological Sciences, Institute for Life Sciences, University of Southampton, Southampton, SO17 1BJ, UK

[b] Diamond Light Source, Harwell Science and Innovation Campus, Didcot, Oxfordshire, OX11 0DE, UK

[c] National Oceanography Centre, Southampton SO14 3ZH, UK

[d] European Synchrotron Radiation Facility, 38043 Grenoble Cedex 9, France

[e] Hamburg Centre for Ultrafast Imaging, HARBOR, Universität Hamburg, Luruper Chaussee 149, 22761 Hamburg, Germany

[f] Randall Centre of Cell and Molecular Biophysics, King's College London, New Hunt's House, Guy's Campus, London, SE1 1UL, UK

[g] MRC Laboratory of Molecular Biology, Francis Crick Avenue, Cambridge Biomedical Campus, Cambridge, CB2 0QH, UK

[h] Laboratory of Biomolecular Research, Paul Scherrer Institute, 5232 Villigen, Switzerland

[i] School of Chemistry, University of Southampton, Southampton, SO17 1BJ, UK

[j] School of Chemistry, University of East Anglia, Norwich NR4 7TJ, UK

[k] Univ. Grenoble Alpes, CNRS, CEA, Institut de Biologie Structurale (IBS), 38044 Grenoble Cedex 9, France

[l] European Molecular Biology Laboratory (EMBL), Hamburg Unit, Notkestraße 85, 22607 Hamburg, Germany

[m] Synchrotron Radiation Life Science Instrumentation Team, RIKEN SPring-8 Center, 1-1-1 Kouto, Sayo, Hyogo 679-5148, Japan

[n] School of Life Sciences, University of Essex, Wivenhoe Park, Colchester CO4 3SQ, UK

[o] National Biofilms Innovation Centre(NBIC), University of Southampton, Southampton, SO17 3DF, UK;

[p] Scottish Association for Marine Science, Oban PA37 1QA, Scotland, UK

[q] Department of Biomedical Sciences, University of Padova, via Ugo Bassi 58/B, 35131 Padova, Italy

[r] Forschungszentrum Jülich GmbH, Jülich Centre for Neutron Science (JCNS), Lichtenbergstraße 1, 85748 Garching, Germany

[s] Research Complex at Harwell, Harwell Science and Innovation Campus, Didcot, OX11 0FA, United Kingdom

[t] Rosalind Franklin Institute, Harwell Science and Innovation Campus, Didcot, Oxfordshire, OX11 0QX, UK

[1]Corresponding author: Ivo Tews, Biological Sciences, Institute for Life Sciences, University of Southampton, Southampton, SO17 1BJ, UK, m: ivo.tews@soton.ac.uk

Email: ivo.tews@soton.ac.uk

Author Contributions: Investigation: RB, MMM, JS, DA, NC, CC, GJT, FMM, SE, EM, TS, AR, MH, RLO, IT; Formal Analysis: RB, JS, DA, NC, LC, MM, MJR, FMM, TS, AR, IT; Methodology: DA, NC, LC, MJR, SE, DvS, TT, HS, JW, RAS, GM, TS, AR, MH, RLO, IT; Funding acquisition: JSW, MZ, SC, AMO, GE, MH, IT; Writing – original draft: RB, MMM, IT, Writing – review & editing: RB, DA, AMO, AR, MH, RLO, IT.

Competing Interest Statement: The authors do not declare competing interests.

Classification: Biological Sciences / Biophysics and Computational Biology.

Keywords: cyanobacteria, serial femtosecond crystallography, radiation damage, iron, ABC transporter.

This file includes:

Main Text
Figures 1 to 4

Abstract

The marine cyanobacterium *Prochlorococcus* is a main contributor to global photosynthesis, whilst being limited by iron availability. Cyanobacterial genomes generally encode two different types of FutA iron binding proteins: periplasmic FutA2 ABC transporter subunits bind Fe(III), while cytosolic FutA1 binds Fe(II). Owing to their small size and their economized genome *Prochlorococcus* ecotypes typically possess a single *futA* gene. How the encoded FutA protein might bind different Fe oxidation states was previously unknown. Here we use structural biology techniques at room temperature to probe the dynamic behavior of FutA. Neutron diffraction confirmed four negatively charged tyrosinates, that together with a neutral water molecule coordinate iron in trigonal bipyramidal geometry. Positioning of the positively charged Arg103 side chain in the second coordination shell yields an overall charge-neutral Fe(III) binding state in structures determined by neutron diffraction and serial femtosecond crystallography. Conventional rotation X-ray crystallography using a home source revealed X-ray induced photoreduction of the iron center with observation of the Fe(II) binding state; here, an additional positioning of the Arg203 side chain in the second coordination shell maintained an overall charge neutral Fe(II) binding site. Dose series using serial synchrotron crystallography and an XFEL X-ray pump-probe approach capture the transition between Fe(III) and Fe(II) states, revealing how Arg203 operates as a switch to accommodate the different iron oxidation states. This switching ability of the *Prochlorococcus* FutA protein may reflect ecological adaptation by genome streamlining and loss of specialized FutA proteins.

Significance Statement

Oceanic primary production by marine cyanobacteria is a main contributor to carbon and nitrogen fixation. *Prochlorococcus* is the most abundant photosynthetic organism on Earth, with an annual carbon fixation comparable to the net global primary production from agriculture. Its remarkable ecological success is based on the ability to thrive in low nutrient waters. To manage iron limitation, *Prochlorococcus* possesses the FutA protein for iron uptake and homeostasis. We reveal a molecular switch in the FutA protein that allows it to accommodate binding of iron in either the Fe(III) or Fe(II) state using structural biology techniques at room temperature and provide a plausible mechanism for iron binding promiscuity.

Main Text

Introduction

Iron is the fourth most abundant element in the Earth's crust (1). However, because of the poor solubility, primary production in large oceanic and freshwater environments is limited by iron uptake (2). In oxygenated aqueous environments, iron predominantly exists in Fe(III) oxyhydroxides (3) with a solubility of 10^{-18} M (4) and consequently precipitates to severely limit bioavailability (5). Marine phytoplankton require iron in the photosynthetic electron transport chain (6) and in the nitrogenase enzyme (7, 8); thus, iron availability directly limits photosynthesis (9) and nitrogen fixation (10).

Cyanobacteria of the *Prochlorococcus* genus are able to fix four gigatons of carbon per annum, which is comparable to the net primary production of global agriculture (11). *Prochlorococcus* bacteria dominate bacterial populations in tropical and subtropical oligotrophic ocean regions (12). One of the factors for ecological success is the exceptional ability of this bacterium to thrive in low nutrient waters (13). Adaptation includes reduction in size to 0.5 – 0.7 μm, making *Prochlorococcus* not only the most abundant but also the smallest photosynthetic organism on Earth (14). Reduction in size maximizes the surface-area-to-volume ratio for metabolic efficiency to a tradeoff of genome reduction, and *Prochlorococcus* maintains the smallest genome (1.6-2.7 Mb) known for any free-living phototroph (15).

Typically, cyanobacteria harbor multiple iron uptake systems (16). In the common TonB transport system, organic ligands (siderophores) are used to solubilize iron (17). The majority of the *Prochlorococcus* species lack genes for siderophore biosynthesis (18, 19); instead, the bacterium relies on the Fut ABC transporter for iron uptake (20). Here, specialized periplasmic proteins sequester elemental iron (16); FutA2 is such a substrate binding protein (SBP) that binds Fe(III) to deliver it to the Fut ABC transporter (21, 22). A functional homologue of FutA2 is the cytosolic protein FutA1 that binds Fe(II) and protects the photosystem against oxidative stress (23-25); however, FutA1 has also been shown to bind Fe(III) (21, 26). We have previously reported dual localization and function for the single FutA protein of the marine cyanobacterium *Trichodesmium* (27), suggesting it can bind both iron species. Similarly, *Prochlorococcus* harbors a single *futA* gene (20), therefore we wanted to understand whether and how a single FutA protein can bind both iron species, and how redox plasticity was structurally encoded.

It is challenging to obtain crystallographic models without alteration of the metal sites, since site-specific damage occurs extremely quickly and at very low doses (28), particularly for iron (29, 30). Indeed, the FutA structure determined from a conventional diffraction experiment on an X-ray home source reported here represented the photo-reduced, Fe(II) binding state, corroborated by spectroscopic evidence. A serial femtosecond crystallography approach (SFX) using an XFEL source and a complementary neutron diffraction approach were required to avoid the manifestations of X-ray induced photoreduction in order to determine the Fe(III) state and give protonation states of iron coordinating amino acid side chains. Using a fixed-target silicon chip system for crystal delivery (31) at both synchrotron and XFEL radiation sources, we studied the transition between Fe(III) to Fe(II) states whilst making use of the effects of X-ray induced photoreduction, varying dose and time. The resulting protein structures support a dual binding mode for iron and give insight into protein adaptation to evolutionary pressures.

Results

The structure of FutA. The crystallographic X-ray structure of FutA was determined from a single crystal to 1.7 Å resolution, using a standard rotation protocol with the crystal in a sealed capillary at a home source setup (**Table S1**). Substrate binding domains such as FutA can be classified based on overall fold and *Prochlorococcus* FutA classifies as “D type” substrate binding protein. The N-terminal (amino acids 1-98 and 232-280, light grey) and C-terminal domains (amino acids 99-231 and 281-314, dark grey) are highlighted in **Fig. 1A**.

The substrate-binding cleft bears the iron-binding site that is open to the surrounding solvent. The four tyrosine side chains of Tyr13 from N-terminal and Tyr143, Tyr199 and Tyr200 from C-terminal domains coordinate the iron, **Fig. 1B**, in this Class IV substrate binding protein (32). The trigonal bipyramidal coordination involves Tyr13, Tyr143 and Tyr200 to form the trigonal plane with iron at its center, while Tyr199 and a coordinating solvent molecule are the axial ligands.

Interestingly, the structure reveals a positioning of two arginine side chains, Arg103 and Arg203, in a second shell around the iron binding site, **Fig. 1C**. One might assume the tyrosine side chains are negatively charged tyrosinates, and arginine side chains would each provide a positive charge, with a neutral solvent molecule. To understand the charge state, we used spectroscopy and confirmed protonation states using neutron diffraction.

Determination of the Fe(III) iron binding state by spectroscopy. A refolding protocol in presence of iron sulfate was used to purify FutA. The burgundy red color of the purified protein that can readily be bleached by excess sodium dithionite likely resulted from the ligand to metal charge transfer (LMCT) bands between the tyrosinate residues coordinating the Fe(III) ion, **Fig. 2A**.

The electron paramagnetic resonance (EPR) spectrum of purified FutA shows a sharp signal at a g-value of 4.29, **Fig. 2B**. This signal is indicative of a $|\pm 3/2\rangle$ doublet from a $3d^5$, high-spin (S = 5/2)

isotropic system (E/D ≈ 1/3), consistent with an Fe(III) ion bound to FutA (33). The weaker signals (g = 5.67, g = 7.90) derive from either $|\pm 1/2\rangle$ ground state transitions or from $|\pm 3/2\rangle$ resonances from rhombic species of the Fe(III) iron. However, given the very high transition probabilities for the g = 4.29 signal compared to the lower transition probability for ground state or anisotropic species, the latter resonances likely represent a significant fraction of the total spins in the sample. Excess of sodium dithionite leads to the loss of the EPR signal, **Fig. 2B**. This could result from loss of iron binding and reduction in solution, or reduction of Fe(III) iron to a colorless and $3d^6$ EPR-silent (probably S=2) Fe(II) state within the active site.

Protonation state of Fe(III) coordinating residues as determined by neutron diffraction. We determined the crystallographic structure of FutA by neutron diffraction to 2.1 Å resolution (**Tables S1 & S2**). Positive density in the neutron F_o-F_c omit map indicates sites of successful hydrogen-deuterium exchange. The lack of difference density on the iron coordinating Tyr13, Tyr143, Tyr199 and Tyr200 suggests these residues are tyrosinates, **Fig. 2C**. The nuclear density for the metal-bound solvent is consistent with neutral water. Arg203 is not engaged in any interactions and does not contribute to the second shell (**Fig. S1A**), in contrast to the X-ray structure, **Fig. 1**. However, the side chain of Arg103 in the second shell is fully protonated and positively charged, thus together with the four negatively charged tyrosinates Fe(III) binding results in an overall charge balanced binding site.

The Fe(III) iron state structure determined by serial femtosecond crystallography (SFX). The SFX experiment used short (10 fs), high-intensity X-ray pulses from the SACLA XFEL to provide diffraction patterns that are collected before the crystal is destroyed (34). It has been shown that data can be recorded free of the effects of radiation induced changes as long as sufficiently short pulses (<20 fs) are used (35). Crystallization conditions were optimized to obtain microcrystal slurries suitable for SFX, as described by us previously (36). For data collection, crystals of approximately 20 x 7 x 7 μm^3 were applied onto a fixed-target silicon chip. Synchronizing chip translation with SACLAs repetition rate of 30 Hz, each aperture was exposed to a single 10 fs XFEL pulse (37). The final dataset was merged from three chips (**Table S1**).

SFX and neutron diffraction structures are similar (see comparison in SI), with the Arg103 side chain contributing to the second shell, but the side chain of Arg203 pointing away from the binding site, **Fig. 2D**. EPR data, neutron diffraction and SFX agree and are consistent with iron binding in the Fe(III) state. In turn, this suggests that the structure determined from the X-ray home source with the Arg203 side chain pointing towards the binding site as shown in **Fig. 1** may represent the Fe(II) state.

Characterization of X-ray induced photoreduction of Fe(III) FutA. The home source rotation experiment might either fortuitously have captured the reduced state, or this observation had resulted from X-ray induced photoreduction of Fe(III) to Fe(II). Photoreduction was highly likely, considering the bleaching of the burgundy-red appearance in the X-ray exposed area of the crystal during data collection. We thus went on to characterize the effect of X-ray exposure using *in crystallo* optical spectroscopy (38).

The electronic absorption peak (λ_{max} = 438 nm) corresponding to the Fe(III) iron (39) progressively decays on incident X-ray irradiation at a synchrotron beamline, **Fig. 3A**. As X-rays induce light-absorbing chemical species in the solvent that overlap with the Fe(III) iron specific signal, the 620 nm wavelength was chosen to minimize the effect of this artefact and characterize photoreduction of the iron center, plotting absorbance against accumulated radiation dose, **Fig. 3B**. Measuring five different crystals, we determined a half-photoreduction dose of 128 ± 21 kGy; the dose at which 80% of the molecules had been photoreduced was 204 ± 27 kGy.

Tracking of X-ray induced photoreduction from an SSX dose series. A fixed target serial synchrotron crystallography (SSX) approach described by us previously (31) is well suited for low dose investigations. A series of ten images with the fixed target remaining stationary was taken

from each microcrystal, where each image incrementally increases the dose, with the fast shutter closed during the advance to the next aperture / crystal position (37). This allowed us to follow structural changes of the FutA iron complex in response to X-ray induced photoreduction.

Two different dose series with dose increments of 5 kGy and 22 kGy are reported (**Tables S3 & S4**). Images corresponding to each dose point are merged to provide a series of datasets corresponding to these dose points. The isomorphous difference density indicates an alternative conformation for Arg203. The feature is readily visible at 22 kGy and strongest at 88 kGy, **Fig. 3C**. Indeed, overlay with the conformation observed in the home source structure, **Fig. 1C**, shows that both structures are similar, suggesting the photoreduced state was observed in either case.

An XFEL X-ray pump-probe (XRPP) approach captures the transition between Fe(III) and Fe(II) states. We designed a novel serial femtosecond crystallography experiment where a first pulse, attenuated using a sapphire wafer mounted on a fast flipper, was followed by a second, unattenuated pulse on the same crystal (**Fig. S2**, see methods and SI**)**. Using SACLA's repetition rate of 30 Hz, the 10 fs pump and probe were spaced 33 ms apart, with no dose delivered between pump and probe due to the pulsed nature of the XFEL source.

While several different levels of attenuation were explored, data for a 350 kGy pump (94% attenuated) yielded structural changes consistent with photoreduction. Interestingly, in contrast to the SSX series, **Fig. 3C**, this experiment preserved the iron coordinating water that was clearly resolved in electron density, **Fig. 4**, consistent with penta-coordinated Fe(II) iron. Ensuing refinement confirms presence of the alternative conformation of Arg203 (**Fig. S3**). For the high occupancy state of Arg203 with the guanidino group closest to the iron center, distances were 4.5 Å between the η1 amide of Arg203 and the phenolate oxygen of Tyr13, and 5.0 Å between the η2 amide of Arg203 and the alkoxy group of Tyr200. The XRPP experiment thus induced specific alteration(s) and created the FutA Fe(II) state *in situ*.

Discussion

The adaptation of the marine cyanobacterium *Prochlorococcus* is a remarkable story of ecological success, making this photosynthetic organism the most abundant on earth. Two factors are particularly important, the ability to survive under limiting nutrient conditions and physical size reduction where both factors put evolutionary pressure on the iron uptake system of the bacterium (13, 14). This study addresses the challenge of how a single gene product, FutA, can bind both Fe(III) and Fe(II) iron.

The structural analyses reported at ambient (room) temperature allow delineating a plausible mechanism for iron binding in two different oxidation states, showing how FutA Arg203 operates as a switch between states. The side chain of this residue is not engaged in polar contacts in the Fe(III) states, which is hinting at its intrinsic dynamics, allowing it to be recruited and engage in interaction with the iron center and contribute a balancing charge in the Fe(II) state, **Fig. 3D**.

X-ray crystallographic study of redox active metallo-proteins is challenging as X-ray induced photoreduction can occur. Transition metals are particularly sensitive to specific radiation damage (28, 40), and observation of the FutA Fe(III) state required SFX or neutron diffraction. Changes in the oxidation state induced by X-rays were previously documented for doses as low as 30 - 20 kGy (30, 37, 41). For Fe(III), we show that the half-point for photoreduction in FutA corresponds to a dose of 128 +/- 21 kGy, as shown by spectroscopic analysis, **Fig. 2B**.

We exploited the effects of X-ray induced photoreduction to study the transition between Fe(III) and Fe(II) states, using a SSX dose series and an SFX X-ray pump probe setup. Compared to previous pump probe approaches (e.g. (35)), time separation of pump and probe pulses is with 33 ms several orders of magnitude larger, allowing us to map conformational changes at ambient temperatures (42) for similar timescales in SSX and SFX XRPP. While both experiments revealed

the alternative conformation for Arg203, density of the coordinating water disappeared with accumulating dose in SSX, **Fig. 3C**, but was preserved in the SFX XRPP approach, **Fig. 4**. The SFX XRPP pump delivered 350 kGy dose in a 10-femtosecond pulse, which was 4 times higher than used in the SSX experiment. The larger beam size of 10 micron for SSX compared to the 1.5 micron for SFX experiments together with the different timescales of irradiation (10ms exposure of the quasi-continuous synchrotron beam and the 10 fs XFEL pulse) would lead to differences in heat load and provided a marked difference for photo-electron escape (43) that was accounted for in dose calculation (SI).

Discovery of a mechanism to bind two different iron oxidation states prompted us to revisit homologues of the FutA iron binding protein, and we found that a similar switch may exist for the iron binding protein FbpA from *Thermus thermophilus* with structures in two states reported (**Fig. S4**). *Synechocystis* has two specialized iron binding proteins, with FutA2 being assigned a Fe(III) binding function in the oxidative environment of the periplasm, while FutA1 binds Fe(II) iron favored under reducing conditions in the cytosol. For these proteins, conservation of the arginine residue equivalent *Prochlorococcus* Arg203 (**Fig. S5**) may relate to biological ability to bind iron at different oxidation states, as discussed in supplementary text.

Conclusion: Structures with iron bound in different oxidation states help explain how the intrinsic structural plasticity of FutA accommodates Fe(II) as well as Fe(III) iron species. Translated into a molecular mechanism, an arginine side chain flip provides a charge balance. The acute sensitivity of FutA to specific radiation damage illustrates the requirement for dose limiting data collection regimes. We have used photoreduction as an advantage to study the transition of Fe(III) to Fe(II) binding state. The X-ray pump probe approach demonstrated here has the potential to become a straightforward-to-implement approach to induce redox state changes probing structural transitions. We envisage that more complex experiments could generate photoreduced states akin to anaerobic conditions that are amenable for further modification by ligand addition.

Materials and Methods

The sections *molecular biology*; *protein purification*; *protein crystallization*; *sample preparation for serial crystallography; crystallographic data processing; structure determination and refinement*; *in crystallo UV-vis spectroscopy* are found in SI. All studies (except EPR) were performed at ambient (room) temperature. Crystallization used the natural pH of the purification buffer (0.1 M Tris buffered at pH 9.0, containing 320 mM NaCl), and 12% (w/v) PEG3350 / 0.2 M NaSCN in vapor diffusion for the home source and in batch for neutron diffraction structures. Seeded batch crystallization with 20% (w/v) PEG3350 / 0.2 M NaSCN was used for serial crystallography. Diffraction-weighted doses (DWD) calculated include photoelectron escape calculation with *RADDOSE-3D* (version 2.1) (44) (for a critical discussion on dose calculation see SI).

Home source crystal structure. Data were collected from a single crystal grown from batch crystallization and measuring 0.23 x 0.24 x 0.12 mm^3, mounted in a 0.7 mm sealed quartz capillary on a Rigaku 007 HF (High Flux) diffractometer equipped with a HyPix 6000HE detector. The X-ray beam with a flux of 2.5 x 10^9 ph/s at 8.1 keV was collimated at 200 μm^2. The total exposure time of 1 hr equated to a total dose of 110 kGy.

Neutron crystallography. For hydrogen-deuterium exchange, Fe(III) loaded FutA crystals grown from batch crystallization were transferred into a deuterated solution of the same crystallization conditions. Two subsequent exchanges, each for 24 hrs, were carried out before crystals with a volume larger than 0.2 mm^3 were mounted in 1 mm sealed quartz capillaries. Data collection at BIODIFF (45), Forschungsreaktor München II (Germany) used a monochromatic neutron beam. The final dataset was merged from two isomorphous crystals collected at wavelengths of 3.1 Å (calibrated to 4DP with an Yttrium Iron Garnet powder sample). Neutron crystallographic refinement was carried out with Refmac5 (46).

Serial synchrotron crystallography (SSX). SSX data were collected at beamline I24, Diamond Light Source, using silicon chips with 12 μm apertures. For each dose series, ten images (10 ms per image) were collected at each aperture. Images were separated into individual dose points for processing to obtain ten dose points (37). Datasets above a total dose of 110 kGy were no longer isomorphous with the lowest dose point, with increased B-factors corroborating global damage.

Serial femtosecond crystallography (SFX). SFX data were collected at SACLA beamline BL2 EH3, Japan, using the MPCCD detector. The XFEL was operated at an X-ray energy of 11.0 keV with a pulse length of 10 fs and a repetition rate of 30 Hz. Synchronizing chip translation with the XFEL pulse, data collection took roughly 14 mins per chip.

SFX X-ray pump probe. For the XRPP experiments, a flipper-attenuator was used to reduce the flux of alternate XFEL pulses. A fast, self-restoring rotary shutter (Branstrom Instruments, USA) mounted upstream of the sample and containing Sapphire wafer in a range of thicknesses was triggered, via TTL from a signal generator, to move the wafer into and out of the X ray beam path. For each pair of pump and probe pulses, the fixed target remained stationary. Pump and probe diffraction images were separated based on total scattering intensity using the dxtbx.radial_average function from the DIALS software package (**Fig. S2**).

UV-vis absorption spectroscopy. In solution spectra were collected in purification buffer (0.1 M Tris buffered at pH 9.0, containing 320 mM NaCl) on a Shimadzu UV-2600 spectrophotometer at a protein concentration of 4.75 mg/ml (0.14 mM). In the chemical reaction experiment, $Na_2S_2O_4$ was added to a final concentration of 1.4 mM under aerobic conditions. *In crystallo* X-ray dose dependent UV-vis absorption spectroscopy was performed at ESRF beamline BM07-FIP2 with a 200 x 200 μm^2 X-ray top-hat beam at 12.66 keV (4.1 and 5.0 x 10^{11} ph/s photon flux). Spectra were acquired at 0.4 Hz with a loop-mount crystal using a humidity controller (HC-Lab, Arinax) (47) bathed in the X-ray beam on an online microspectrophotometer with a focal volume of 50 x 50 x ~100 μm^3 (38, 48).

Electron paramagnetic resonance. FutA at a concentration of 50 μM was shock-frozen in liquid nitrogen. In the chemical reduction experiment, $Na_2S_2O_4$ was added to a final concentration of 500 μM under aerobic conditions prior to freezing. Data collection was carried out in EPR quartz tubes at liquid helium temperature. X-band continuous wave EPR spectra (10 Gauss modulation amplitude, 2 mW microwave power) were recorded on a Bruker eleXsys E500 spectrometer using a standard rectangular Bruker EPR cavity (ER4102T) equipped with an Oxford helium cryostat (ESR900) at 5 – 6 K.

Acknowledgments

We thank Chris Holes for macromolecular crystallization, Peter Horton for diffraction, and Peter Roach for critical discussion at the University of Southampton (UoS). Financial support: Japan Partnering Award, Biological Sciences Research Council (BBSRC) BB/R021015/1, BB/W001950/1 to JW, MH, RO; Diamond Doctoral Studentship Programme to RB, JS, MR, CC; South Coast Biosciences Doctoral Training Partnership SoCoBio DTP BBSRC BB/T008768/1 to JS; PhD studentships by Hamburg University and the European Synchrotron Radiation Facility (ESRF) to NC, the Collaborative Computing Project 4 (CCP4) to LC (#7920S22020007); the Institute for Life Sciences (Southampton) to CC; BBSRC BB/X002950/1 “The National Biofilms Innovation Centre (NBIC)” to J.S.W.; Wellcome Investigator Award 210734/Z/18/Z to AMO; Royal Society Wolfson Fellowship RSWF\R2\182017 to AMO. We acknowledge facility access to the National Crystallography Service (NCS) Southampton; DLS MX15722, NT14493, NT23570; SACLA 2022A8002, 2022B8041; Forschungsreaktor München ID:16106; ESRF BM07-FIP2 and *ic*OS, MX2373, MX2374; Diamond Light Source (DLS) UK XFEL hub and ESRF for travel support. We are grateful to beamline staff, in particular Shigeki Owada and Kensuke Tono at SACLA.

References

1. K. Hans Wedepohl, The composition of the continental crust. *Geochimica et Cosmochimica Acta* **59**, 1217-1232 (1995).
2. P. W. Boyd *et al.*, Mesoscale Iron Enrichment Experiments 1993-2005: Synthesis and Future Directions. *Science* **315**, 612-617 (2007).
3. W. Stumm, B. Sulzberger, The cycling of iron in natural environments: Considerations based on laboratory studies of heterogeneous redox processes. *Geochimica et Cosmochimica Acta* **56**, 3233-3257 (1992).
4. M. L. Wells, N. M. Price, K. W. Bruland, Iron chemistry in seawater and its relationship to phytoplankton: a workshop report. *Marine Chemistry* **48**, 157-182 (1995).
5. H. W. Rich, F. M. M. Morel, Availability of well-defined iron colloids to the marine diatom Thalassiosira weissflogii. *Limnology and Oceanography* **35**, 652-662 (1990).
6. J. A. Raven, M. C. W. Evans, R. E. Korb, The role of trace metals in photosynthetic electron transport in O2-evolving organisms. *Photosynthesis Research* **60**, 111-150 (1999).
7. S. Richier *et al.*, Abundances of Iron-Binding Photosynthetic and Nitrogen-Fixing Proteins of Trichodesmium Both in Culture and In Situ from the North Atlantic. *PLoS ONE* **7**, e35571 (2012).
8. J. T. Snow *et al.*, Quantifying Integrated Proteomic Responses to Iron Stress in the Globally Important Marine Diazotroph Trichodesmium. *PLOS ONE* **10**, e0142626 (2015).
9. Z. S. Kolber *et al.*, Iron limitation of phytoplankton photosynthesis in the equatorial Pacific Ocean. *Nature* **371**, 145-149 (1994).
10. M. C. Moore *et al.*, Large-scale distribution of Atlantic nitrogen fixation controlled by iron availability. *Nature Geoscience* **2**, 867-871 (2009).
11. M. A. Huston, S. Wolverton, The global distribution of net primary production: resolving the paradox. *Ecological Monographs* **79**, 343-377 (2009).
12. P. Flombaum *et al.*, Present and future global distributions of the marine cyanobacteria Prochlorococcus and Synechococcus. *Proceedings of the National Academy of Sciences* **110**, 9824-9829 (2013).
13. S. J. Biller, P. M. Berube, D. Lindell, S. W. Chisholm, Prochlorococcus: the structure and function of collective diversity. *Nature Reviews Microbiology* **13**, 13-27 (2015).
14. F. Partensky, W. R. Hess, D. Vaulot, Prochlorococcus, a Marine Photosynthetic Prokaryote of Global Significance. *Microbiology and Molecular Biology Reviews* **63**, 106-127 (1999).
15. P. M. Berube *et al.*, Single cell genomes of Prochlorococcus, Synechococcus, and sympatric microbes from diverse marine environments. *Sci Data* **5**, 180154 (2018).
16. R. Sutak, J.-M. Camadro, E. Lesuisse, Iron Uptake Mechanisms in Marine Phytoplankton. *Frontiers in Microbiology* **11** (2020).
17. M. Sandy, A. Butler, Microbial Iron Acquisition: Marine and Terrestrial Siderophores. *Chem Rev* **109**, 4580-4595 (2009).
18. D. B. Rusch, A. C. Martiny, C. L. Dupont, A. L. Halpern, J. C. Venter, Characterization of Prochlorococcus clades from iron-depleted oceanic regions. *Proceedings of the National Academy of Sciences* **107**, 16184-16189 (2010).
19. R. R. Malmstrom *et al.*, Ecology of uncultured Prochlorococcus clades revealed through single-cell genomics and biogeographic analysis. *International Society for Microbial Ecology Journal* **7**, 184-198 (2013).
20. G. Rocap *et al.*, Genome divergence in two Prochlorococcus ecotypes reflects oceanic niche differentiation. *Nature* **424**, 1042-1047 (2003).
21. H. Katoh, N. Hagino, A. R. Grossman, T. Ogawa, Genes essential to iron transport in the cyanobacterium Synechocystis sp. strain PCC 6803. *Journal of Bacteriology* **183**, 2779-2784 (2001).
22. A. Badarau *et al.*, FutA2 is a ferric binding protein from Synechocystis PCC 6803. *Journal of Biological Chemistry* **283**, 12520-12527 (2007).

23. P. Exss-Sonne, J. Tölle, K. P. Bader, E. K. Pistorius, K.-P. Michel, The IdiA protein of Synechococcus sp. PCC 7942 functions in protecting the acceptor side of Photosystem II under oxidative stress. *Photosynthesis Research* **63**, 145-157 (2000).
24. J. Tölle *et al.*, Localization and function of the IdiA homologue Slr1295 in the cyanobacterium Synechocystis sp. strain PCC 6803. *Microbiology* **148**, 3293-3305 (2002).
25. K. P. Michel, E. K. Pistorius, Adaptation of the photosynthetic electron transport chain in cyanobacteria to iron deficiency: The function of IdiA and IsiA. *Physiologia Plantarum* **120**, 36-50 (2004).
26. H. Katoh, N. Hagino, T. Ogawa, Iron-binding activity of FutA1 subunit of an ABC-type iron transporter in the cyanobacterium Synechocystis sp. Strain PCC 6803. *Plant and Cell Physiology* **42**, 823-827 (2001).
27. D. Polyviou *et al.*, Structural and functional characterization of IdiA/FutA (Tery_3377), an iron-binding protein from the ocean diazotroph Trichodesmium erythraeum. *Journal of Biological Chemistry* **293**, 18099-18109 (2018).
28. E. F. Garman, M. Weik, Radiation Damage in Macromolecular Crystallography. *Methods Mol Biol* **1607**, 467-489 (2017).
29. J. A. R. Worrall, M. A. Hough, Serial femtosecond crystallography approaches to understanding catalysis in iron enzymes. *Curr Opin Struc Biol* **77** (2022).
30. V. Pfanzagl *et al.*, X-ray–induced photoreduction of heme metal centers rapidly induces active-site perturbations in a protein-independent manner. *Journal of Biological Chemistry* **295**, 13488-13501 (2020).
31. S. Horrell *et al.*, Fixed Target Serial Data Collection at Diamond Light Source. *J Vis Exp* 10.3791/62200 (2021).
32. S. Wang *et al.*, A novel mode of ferric ion coordination by the periplasmic ferric ion-binding subunit FbpA of an ABC-type iron transporter from Thermus thermophilus HB8. *Acta Crystallographica Section D* **70**, 196-202 (2014).
33. G. Palmer, The electron paramagnetic resonance of metalloproteins. *Biochem Soc Trans* **13**, 548-560 (1985).
34. H. N. Chapman, X-Ray Free-Electron Lasers for the Structure and Dynamics of Macromolecules. *Annu Rev Biochem* **88**, 35-58 (2019).
35. K. Nass *et al.*, Structural dynamics in proteins induced by and probed with X-ray free-electron laser pulses. *Nat Commun* **11**, 1814 (2020).
36. J. H. Beale *et al.*, Successful sample preparation for serial crystallography experiments. *Journal of Applied Crystallography* **52**, 1385-1396 (2019).
37. A. Ebrahim *et al.*, Dose-resolved serial synchrotron and XFEL structures of radiation-sensitive metalloproteins. *International Union of Crystallography Journal* **6**, 543-551 (2019).
38. D. von Stetten *et al.*, In crystallo optical spectroscopy (icOS) as a complementary tool on the macromolecular crystallography beamlines of the ESRF. *Acta Crystallogr D Biol Crystallogr* **71**, 15-26 (2015).
39. A. M. Orville, N. Elango, J. D. Lipscomb, D. H. Ohlendorf, Structures of competitive inhibitor complexes of protocatechuate 3,4-dioxygenase: multiple exogenous ligand binding orientations within the active site. *Biochemistry* **36**, 10039-10051 (1997).
40. M. A. Hough, R. L. Owen, Serial synchrotron and XFEL crystallography for studies of metalloprotein catalysis. *Curr Opin Struct Biol* **71**, 232-238 (2021).
41. I. G. Denisov, D. C. Victoria, S. G. Sligar, Cryoradiolytic reduction of heme proteins: Maximizing dose-dependent yield. *Radiation Physics and Chemistry* **76**, 714-721 (2007).
42. J. S. Fraser *et al.*, Accessing protein conformational ensembles using room-temperature X-ray crystallography. *Proc Natl Acad Sci U S A* **108**, 16247-16252 (2011).
43. S. L. S. Storm *et al.*, Measuring energy-dependent photoelectron escape in microcrystals. *IUCrJ* **7**, 129-135 (2020).
44. C. S. Bury, J. C. Brooks-Bartlett, S. P. Walsh, E. F. Garman, Estimate your dose: RADDOSE-3D. *Protein Science* **27**, 217-228 (2018).

45. T. S. A. Ostermann, BIODIFF: Diffractometer for large unit cells. *Journal of large-scale research facilities* **1**, A2 (2015).
46. L. Catapano *et al.*, Neutron crystallographic refinement with REFMAC5 from the CCP4 suite. *Acta Crystallogr D Struct Biol* **79**, 1056-1070 (2023).
47. J. Sanchez-Weatherby *et al.*, Improving diffraction by humidity control: a novel device compatible with X-ray beamlines. *Acta Crystallogr D Biol Crystallogr* **65**, 1237-1246 (2009).
48. J. McGeehan *et al.*, Colouring cryo-cooled crystals: online microspectrophotometry. *J Synchrotron Radiat* **16**, 163-172 (2009).

Figures and Tables

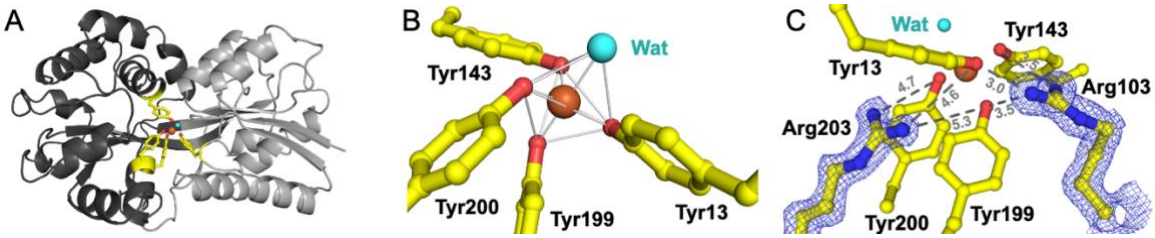

Figure 1. The Fe(II) state FutA structure from an X-ray home source determined to 1.7 Å resolution. (*A*) FutA has a bi-lobal structure with the substrate binding cleft between the N-terminal (light grey) and C-terminal domains (dark grey). Amino acid side chains contributing to iron binding are shown in stick representation (yellow). (*B*) Trigonal bipyramidal coordination of the iron, with Tyr199 and a solvent molecule as axial ligands. (*C*) The two arginine side chains of Arg103 and Arg203 are in a second coordination shell, shown here with refined density ($2F_{obs} - F_{calc}$, blue map, contoured at 1.5 σ). Color coding is yellow for carbon, red for oxygen, blue for nitrogen, orange for iron, with the solvent molecule in light blue.

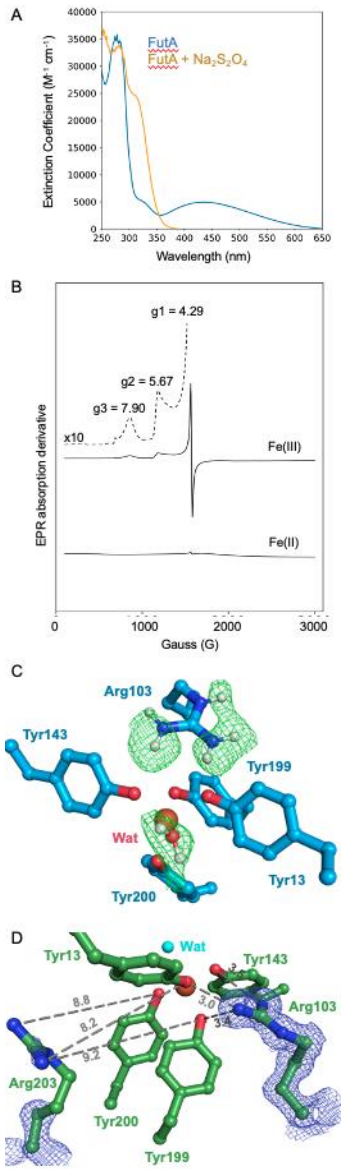

Figure 2. The FutA Fe(III) state characterized by UV-vis and EPR spectroscopy, neutron diffraction and serial femtosecond crystallography. (*A*) The UV-vis spectrum of recombinantly produced and purified FutA (blue) shows an absorbance maximum at 438 nm, consistent with Fe(III) bound to FutA. The peak at 438 nm disappears after addition of 10-fold molar excess sodium dithionite; the absorbance maximum at 315 nm indicates free sodium dithionite (yellow). (*B*) EPR spectrum of purified and sodium dithionite reduced FutA. The peaks observed were: g1 = 4.29 g, g2 = 5.67 g, g3 = 7.9 g. (*C*) The positive nuclear density in the neutron diffraction crystal structure (green mesh, $F_{obs} - F_{calc}$ omit map at 3σ, 2.1 Å resolution) indicates sites that have undergone hydrogen-deuterium exchange, showing an oriented water as axial ligand (refined deuterium fraction > 0.80). Arg103 fully protonated and positively charged, while the four tyrosine side chains do not show difference density, suggesting they are negatively charged tyrosinates. (*D*) The SFX crystal structure shows that the side chain of Arg203 is not oriented towards the binding site and does not engage in polar interactions (similar to the neutron diffraction structure **Fig. S1**). Carbons shown blue (neutron diffraction) or green (SFX), heteroatoms colored as in **Fig. 1**.

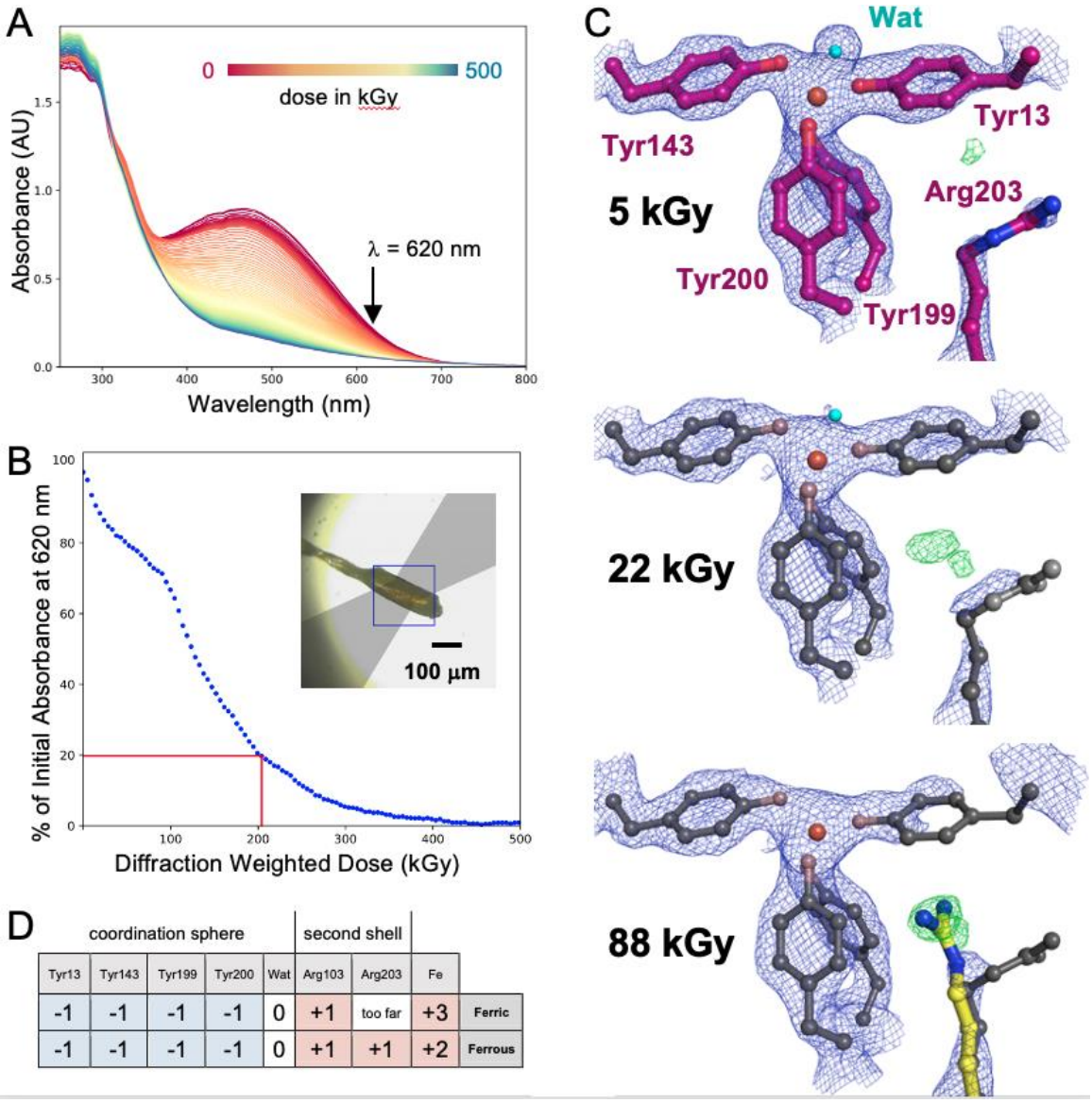

D

coordination sphere					second shell			
Tyr13	Tyr143	Tyr199	Tyr200	Wat	Arg103	Arg203	Fe	
-1	-1	-1	-1	0	+1	too far	+3	Ferric
-1	-1	-1	-1	0	+1	+1	+2	Ferrous

Figure 3. X-ray induced photoreduction of FutA characterized by spectroscopy and SSX. (*A*) Successive UV-vis absorption spectra collected *in crystallo* plotted for a FutA crystal during X-ray exposure, from 0 kGy (red) to 500 kGy (blue). Photoreduction was monitored at a wavelength of 620 nm (arrow). (*B*) Evolution of the normalized absorbance at 620 nm, collected on a single crystal. In the example shown, 80% of the signal was lost at 204 ± 27 kGy (red lines). Inset: geometry of the experiment. The light path for the spectroscopic measurement is indicated in grey. (*C*) SSX dose series at RT. Top: refined structure at 5 kGy (carbon atoms shown in purple; 2Fo-Fc density in blue contoured at 1.5 σ, Fo-Fc in green contoured at 3 σ). Pronounced difference density is seen at 22 kGy and 88 kGy, suggesting Arg203 takes an alternative conformation, as indicated by overlay with the conformation seen in the Fe(II) state determined from the home source (Arg203 carbons shown in yellow for the 88 kGy dose point). Heteroatoms colored as in **Fig. 1**. (*D*) Charges of amino acids contributing to the coordination sphere and second shell for the Fe(III) and Fe(II) binding states, assuming an overall neutral state of the binding site.

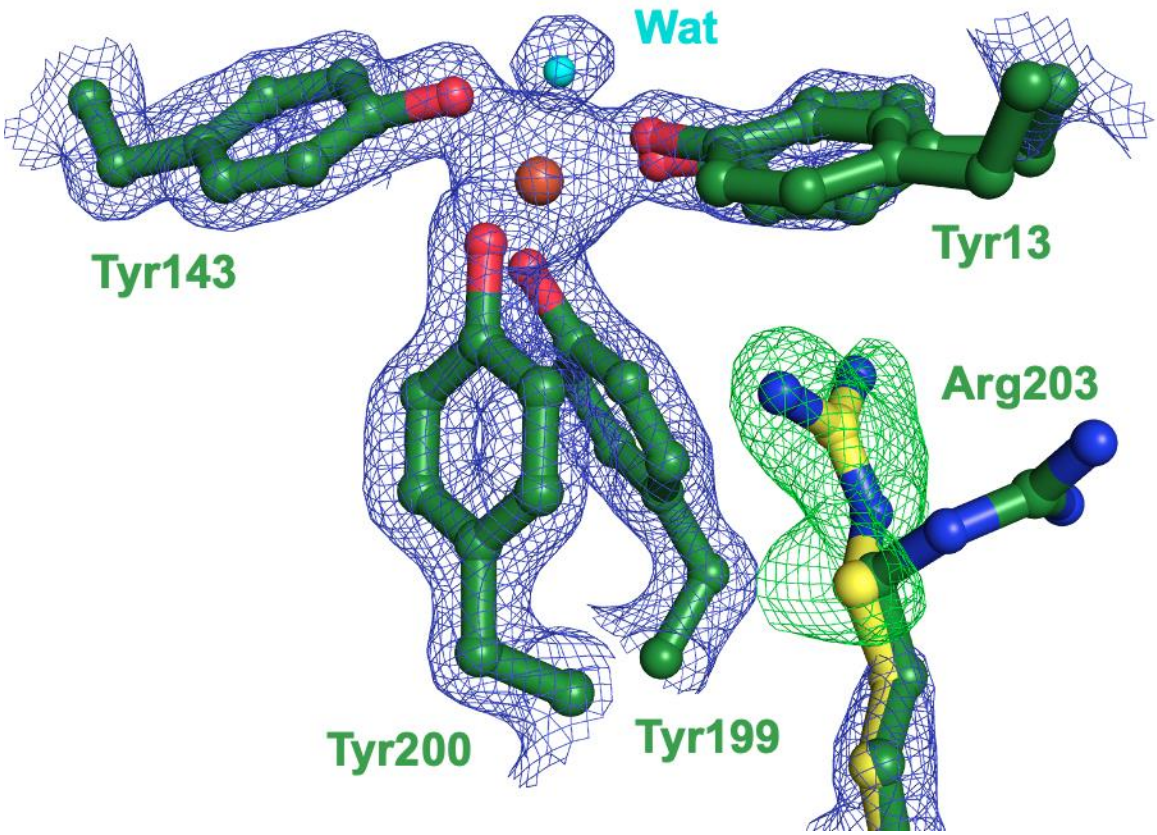

Figure 4. SFX X-ray pump probe experiment. The model of the Fe(III) iron state determined SFX (compare **Fig. 2D**) was used in refinement against an SFX probe dataset, collected after a 350 kGy pump. Refined electron density shows Tyr13 in a double conformation, but limited density for the Arg203 guanidino group (2Fo-Fc, blue, 1.5 σ); however, difference density (Fo-Fc, green, 3 σ) suggests that Arg203 takes an alternative conformation similar to the conformation observed in the Fe(II) state determined from the home source (Arg203 carbons shown in yellow). Heteroatoms colored as in **Fig. 1**.

PNAS

Supplement for

A redox switch allows binding of Fe(II) and Fe(III) ions in the cyanobacterial iron binding protein FutA from *Prochlorococcus*

Rachel Bolton[a,b], Moritz M. Machelett[a,c], Jack Stubbs[a,b], Danny Axford[b], Nicolas Caramello[d,e], Lucrezia Catapano[f,g], Martin Malý[a], Matthew J. Rodrigues[a,b,h], Charlotte Cordery[a,b], Graham J. Tizzard[i], Fraser MacMillan[j], Sylvain Engilberge[d,k], David von Stetten[l], Takehiko Tosha[m], Hiroshi Sugimoto[m], Jonathan A.R. Worrall[n], Jeremy S. Webb[a,o], Mike Zubkov[c,p], Simon Coles[i], Eric Mathieu[k], Roberto A. Steiner[f,q], Garib Murshudov[g], Tobias E. Schrader[r], Allen M. Orville[b,s], Antoine Royant[d,k], Gwyndaf Evans[b,t], Michael A. Hough[b,n,s], Robin L. Owen[b], Ivo Tews[a,1]

[a] Biological Sciences, Institute for Life Sciences, University of Southampton, Southampton, SO17 1BJ, UK; [b] Diamond Light Source, Harwell Science and Innovation Campus, Didcot, Oxfordshire, OX11 0DE, UK; [c] National Oceanography Centre, Southampton SO14 3ZH, UK; [d] European Synchrotron Radiation Facility, 38043 Grenoble Cedex 9, France; [e] Hamburg Centre for Ultrafast Imaging, HARBOR, Universität Hamburg, Luruper Chaussee 149, 22761 Hamburg, Germany; [f] Randall Centre of Cell and Molecular Biophysics, King's College London, New Hunt's House, Guy's Campus, London, SE1 1UL, UK; [g] MRC Laboratory of Molecular Biology, Francis Crick Avenue, Cambridge Biomedical Campus, Cambridge, CB2 0QH, UK; [h] Laboratory of Biomolecular Research, Paul Scherrer Institute, 5232 Villigen, Switzerland; [i] School of Chemistry, University of Southampton, Southampton, SO17 1BJ, UK; [j] School of Chemistry, University of East Anglia, Norwich NR4 7TJ, UK; [k] Univ. Grenoble Alpes, CNRS, CEA, Institut de Biologie Structurale (IBS), 38044 Grenoble Cedex 9, France; [l] European Molecular Biology Laboratory (EMBL), Hamburg Unit, Notkestraße 85, 22607 Hamburg, Germany; [m] Synchrotron Radiation Life Science Instrumentation Team, RIKEN SPring-8 Center, 1-1-1 Kouto, Sayo, Hyogo 679-5148, Japan; [n] School of Life Sciences, University of Essex, Wivenhoe Park, Colchester CO4 3SQ, UK; [o] National Biofilms Innovation Centre(NBIC), University of Southampton, Southampton, SO17 3DF, UK; [p] Scottish Association for Marine Science, Oban PA37 1QA, Scotland, UK; [q] Department of Biomedical Sciences, University of Padova, via Ugo Bassi 58/B, 35131 Padova, Italy; [r] Forschungszentrum Jülich GmbH, Jülich Centre for Neutron Science (JCNS), Lichtenbergstraße 1, 85748 Garching, Germany; [s] Research Complex at Harwell, Harwell Science and Innovation Campus, Didcot, OX11 0FA, United Kingdom; [t] Rosalind Franklin Institute, Harwell Science and Innovation Campus, Didcot, Oxfordshire, OX11 0QX, UK

[1]Corresponding author: Ivo Tews, Biological Sciences, Institute for Life Sciences, University of Southampton, Southampton, SO17 1BJ, UK, m: ivo.tews@soton.ac.uk

This supplement includes:

Extended Materials and Methods

Molecular biology. Prochlorococcus MED4 *futA* was cloned into pET-24b(+) using the NdeI / HindIII restriction sites, excluding the region encoding the N-terminal signal peptide, amino acids 27-340 (UniProt ID: Q7V0T9) as predicted by *SignalP* (1).

Protein purification. Transformed *Escherichia coli* BL21 (DE3) cells (NEB) were cultured in 3 L baffled flasks in 1 L lysogeny broth containing 50 μg ml^{-1} kanamycin, and incubated in a shaker at 130 RPM, 37 °C. The temperature was reduced to 18 °C when the cell culture reached an OD_{600} of 0.4. Protein expression was induced at an OD_{600} of ~0.6 by addition of IPTG (final concentration 1 mM). Cells were harvested after 20 hrs by centrifugation at 4000 x g (Avanti Jxn-26, JLA-8.1000 rotor). Cell pellets (2-4g) were resuspended in 25 ml IBB buffer (0.1 M Tris buffered at pH 9, containing 0.5 M NaCl, 1% Triton-X, 5 mM $MgCl_2$ and 10 mM β-mercaptoethanol). For lysis 2 mg ml^{-1} lysozyme was added, and cells were left for 30 min before sonication for total pulse time of 150 seconds (Q700 Sonicator, 10 second pulse duration with 20 seconds between pulses). Inclusion bodies were harvested by centrifugation (40 mins, 125 000 x g, 4 °C, Optima XPN-80, Type 70 Ti rotor). The pellet was washed in IBB containing 2 M urea, followed by centrifugation (as above). Solubilization was carried out by incubation in 200 mM Tris buffered at pH 9, containing 6 M urea, 10 mM β-mercaptoethanol (1 hrs, 4 °C). After removing cellular debris by centrifugation (as above), a rapid dilution protocol was carried out to refold the protein. The solute was loaded into a syringe with a fine needle and slowly added directly into 2 L of stirring 0.2 M Tris buffered at pH 9.0, containing 0.2 M NaCl, 0.4 M L-Arginine and 0.1 mM $NH_4Fe(SO_4)_2$. After incubation at 4 °C for 48 h, the refolding buffer was concentrated to 150 ml using an Amicon Stirred Cell (10,000 Da Ultrafiltration Disk, Merck). Dialysis against 2 L 100 mM Tris buffered at pH 9.0, containing 145 mM NaCl for 24 hrs at 4 °C was followed by capture on a 5 ml HiTrap SP XL column (GE Healthcare) at room temperature. Step-elution with 0.1 M Tris buffered at pH 9.0, containing 320 mM NaCl was followed by size-exclusion chromatography on a HiLoad 16/60 Superdex 200 column (GE Healthcare) using 50 mM Tris buffered at pH 9.0, containing 300 mM NaCl at room temperature. Fractions containing monomeric FutA were pooled and concentrated using a Vivaspin 20 Centrifugal Concentrator, MWCO 10,000 Da (Sartorius) at 4 °C and stored at 4 °C or room temperature.

Protein Crystallization. FutA at a concentration of ~50 mg ml^{-1} was crystallized at room temperature at the final pH from purification (pH 9.0). The specific crystallization conditions used for each dataset described are described in the main manuscript, all crystals were burgundy red. FutA typically crystallized at a range of precipitant concentrations. For vapor diffusion crystallization, 1 μl protein was mixed with 1 μl 0.2 M sodium thiocyanate containing 10 - 35 % (w/v) PEG 3350 and set up in 24-well XRL plates (Molecular Dimensions). Crystals with 10 – 200 μm in the longest dimension appeared within 1 day. For the home source and neutron diffraction experiments, batch crystallization was used where 10 μl of protein was mixed with 10 μl of 0.2 M sodium thiocyanate containing 12 % (w/v) PEG 3350 in a microcentrifuge tube. Crystals with 200 – 1500 μm in the longest dimension appeared within 3 days. For serial crystallography, seeded batch crystallization was used where seeds were generated by mixing 10 μl of FutA crystals obtained from vapor diffusion droplets with 40 μl 20% PEG 3350, followed by vortexing with Seed Bead for 180 s (Hampton Research). Seed stock aliquots (5 μl) were shock frozen and diluted 1:100 with 0.2 M sodium thiocyanate, 20 % (w/v) PEG 3350 prior to use. For crystallization, 50 μl protein was mixed with 75 μl diluted seed stock and 75 μl of 0.2 M sodium thiocyanate containing 20 % (w/v) PEG 3350. Crystals with 10 – 20 μm in the longest dimension appeared within 30 minutes as described previously (2).

Sample preparation for serial crystallography. Optimization of crystallization for serial crystallography was described previously (2). We used a fixed-target silicon chip, each accommodating 25,600 apertures, to deliver microcrystals to the X-ray interaction region (3). The crystal slurry (typically 150 μl) was loaded onto a glow-discharged chip containing 7 or 12 μm sized apertures within a humidity-controlled chamber, collected by applying vacuum, and sealing

the chip between two sheets of 6 μm thick Mylar. Crystal slurries had to be prepared directly before the experiment to avoid crystal ageing that manifested as loss of diffraction.

Crystallographic data processing, structure determination and refinement. Data collection for all datasets was performed at ambient (room) temperature, with data collection and refinement statistics as given in **Table S1**. The SFX 5 kGy and XRPP 350 kGy datasets show higher B-values than the other three datasets, likely rooted in de/hydration effects of the fixed target chip mount and through incident X-ray irradiation, in particular in the XRPP experiment. The ambient temperature where the data was collected is reported, and the XFEL experiments were conducted at the higher temperature of 25 °C . The home source diffraction data were integrated with *XDS* (4), and scaled / merged using *POINTLESS* and *AIMLESS* (5). The Neutron diffraction data were integrated using *HKL2000* (6) and scaled / merged using *SCALEPACK* (6). The diffraction data for the SSX dose series was indexed and integrated using *dials.stills_process* (*DIALS* v2.0) (7) and scaled using *cctbx.prime* (8). Results for two dose-series are shown in **Table S2**, using 5 kGy and 22 kGy dose-slicing. B-factor sharpening was applied in scaling to correct for the increase in B-factors in each series. *SCALEit* (9) was used to derive the isomorphous difference between two datasets (D_{iso}), and scale the differences in observed structure factors between datasets. SFX diffraction data were stored in a hdf5 stream, applying indexing and pre-filtering for diffraction hits with *Cheetah* (10). Diffraction hits were indexed and integrated with *dials.stills_process* (*DIALS* v3.0) (7). An image mask was generated manually using *dials.image_viewer* to remove the beam stop shadow and monocrystalline Si diffraction spots arising from the chips. Integrated patterns were scaled and merged using the *DIALS* module *cctbx.xfel.merge* (11). Molecular replacement with *MOLREP* (12) used the *Synechocystis* PCC 6803 FutA2 as search model (PDB: 2PT1). *COOT* (13), and *REFMAC5 (14, 15)* were used for iterative model building, refinement and validation. Coordinates and structure factors were deposited with the PDB under accession numbers 8OEM (Home Source), 8RK1 (Neutron), 8C4Y (SFX), 8OGG (SSX 5 kGy), and 8OEI (SFX 350kGy), using the EBI validation suite.

In crystallo UV-vis spectroscopy. Online micro spectrophotometry at beamline ESRF BM07-FIP2 used 400 μm optical fibre to connect a balanced deuterium-halogen lamp (Mikropack DH2000-BAL, Ocean Optics) to the higher objective, while a 600 μm optical fibre connected the lower objective to a fixed-grating spectrophotometer equipped with a CCD detector (QE65 Pro, Ocean Optics). Spectra were acquired at 0.4 Hz (250 ms acquisition time averaged 10 times) on several crystals with a volume between 160 x 70 x 50 μm^3 and 200 x 90 x 80 μm^3. Crystals were oriented to optimize the signal-to-noise ratio of the spectra and maintained still during X-ray exposure in a loop-mount using a humidity controller (HC-Lab, Arinax) (16). Data analysis was performed using a suite of in-house Python scripts (https://github.com/ncara/icOS) with the *NumPy* (17), *pandas* (18), *SciPy* (19) and *Matplotlib* (20) packages. Spectra were first baseline-corrected by subtraction of a constant corresponding to the average absorption between 800 and 880 nm. They were then smoothed using a Savitzky-Golay filter (parameters: 3rd order polynomial; 25-data point smoothing window).

Supplementary Text

Comparison of the iron coordination in the neutron diffraction and SFX structures.

Further investigation of the iron binding site was carried out by performing refinement runs of the neutron diffraction and SFX models using REFMAC5 (15). The latest procedure implemented in REFMAC5 available in CCP4 8.0 includes the refinement of structures obtained by neutron diffraction (14).

Crystallographic refinement was carried out using two alternative strategies. In a first approach, refinement was performed without restraints between the iron center and its coordination ligands. In a second approach, restraints were employed between the metal center and its four coordinating tyrosine residues (Tyr13, Tyr143, Tyr199, Tyr200). Restraint values were derived from the Crystallography Open Database (COD) (21), and two Fe-O target values (1.800 Å and

Fe-O = 2.004 Å) were tested. In the latter approach we also utilized four different weights for the Fe-O restraints with sigma values ranging from 0.01 Å (tight) to 0.04 Å (soft). Coordination distances following refinement are reported in **Table S2**. The final models were refined without restraints between iron and coordinating residues (no link).

It appeared that, whilst Fe-ligand distances in the SFX structure were rather insensitive to the restraints and sigma values employed, those for the NMX model exhibit a behavior that is more biased toward the chosen target value. This is in keeping with lower resolution and completeness of the NMX data (2.1 Å and 81%, respectively) compared to the SFX experiment (1.6 Å and 99.8 %, respectively), resulting in differences of the coordinate error. The precision of placement was calculated to be ±0.294 Å for NMX and ±0.109 Å for SFX with the program SPBS (22) using the web server at https://cluster.physics.iisc.ernet.in/sbps.

In general, differences in apparent distances are to be expected as NMX reports on the position of the atomic nuclei whilst X-ray methods report on the electron distribution. In the specific case, the electron cloud of oxygen is expected to be drawn to and extend towards the positively charged iron-center. The average coordination distance was with 2.09 Å larger for the NMX model (PDB:8RK1) than that for the SFX model with 1.93 Å (PDB:8C4Y). The Fe-water distance that was ~0.2 Å larger in the NMX model than in the SFX model, **Fig. S1B**. The neutron structure additionally features a water molecule not seen in the SFX model in H-bonding distance to the iron coordinating water.

Discussion of dose calculation

Raddose-3D was used in all cases with inclusion of calculation of photoelectron escape, this being the best available tool to estimate dose (23). For SFX XRPP, RADDOSE-3D rather than RADDOSE-XFEL (24) was used as we were probing the effects of the total dose deposited by the pump pulse 33 milliseconds after the pulse rather than the time resolved evolution of dose within the duration of the pulse. Diffraction-weighted doses (DWD) were calculated in all cases since it is a common metric to compare data from different sources.

In this communication we describe differences in metal coordination based on dose. However, we accept that the different regimen described in the experiments could lead to the different observations. In the case of the SFX experiment, the beam was small with respect to the crystal, leading to the X-ray exposed region being surrounded by a large nonexposed crystal volume. In the SSX experiment the crystal is bathed in the beam (at least in two dimensions, as FutA crystals have an axis ratio of typ. 2.5:1:1). X-ray exposure at an XFEL differs from the more conventional SSX experiment by twelve orders of magnitude. The home source experiment did differ in beam and crystal size, but also in incident photon flux and the duration of the experiment. The difference in the behavior of the iron coordinating water between the home source, SSX, and SFX XRPP experiments could be attributed to differences in hygroscopic stability of the sample delivery systems (quartz capillary vs mylar sealed chip) or possible dehydration differences between the individual crystal preparations.

The mechanisms by which redox chemistry plays out in the XRPP experiment after the first 10fs XFEL pulse may well be rather different to a conventional experiment at a synchrotron source with a constant X-ray exposure. Generally, it is the production of solvated photoelectrons from radiolysis of water molecules within the crystal that primarily drive dose-dependent reduction of redox centres. The cascade of reactions leading to production of these photoelectrons however may well be different in these two scenarios. While under cryogenic conditions radiation damage has been shown to be (essentially) purely dose dependent, at room temperature there are clearly time-dependent processes occurring as a result of X-ray exposure, as well as dose driven processes.

For the optical spectroscopic data, we also used DWD to allow comparableness, but we note that a spectroscopic experiment performed on a crystallography beamline with a top-hat-shaped

beam irradiating a still crystal would rather use the ADER metric (Average Dose over the Exposed Region), since doses corresponding to successive spectra increase linearly with exposure time. In contrast, the DWD of an oscillation experiment takes into account that the first images “see” fewer X-rays than the ones at the end of the experiment (24). Calculated as ADER, doses would approximately double for the spectroscopic experiment with a top-hat-shaped X-ray beam. It was previously discussed that ADER might be used when microcrystals and microbeams are used (25), though it is presently unclear how the XRPP data should be treated.

Analysis of sequence conservation in the iron binding site of FutA proteins

The data in this manuscript suggest that *Prochlorococcus* MED4 FutA can bind iron in the Fe(III) and in the Fe(II) redox states, using an arginine switch mechanism. This observation raises the question whether this concept can be extended to other FutA homologues. We therefore carried out multiple sequence alignment analysis (MSA) across a set of known FutA homologues, **Fig. S5**.

The bacterial species selected here are gram-negative, free-living marine bacteria that are found in oligotrophic ocean waters. Of these, *Prochlorococcus* MED4 and *Synechocystis* PCC 6803 are capable of carbon fixation, whereas *T. erythraeum* and *C. chwakensis* are also capable of nitrogen fixation. *T. thermophilus* is a heterotrophic, extremophile, isolated from deep-sea thermal vents. Species with a single FutA homologue in their genome were *Prochlorococcus* MED4 (UniProt ID: Q7V0T9), *Trichodesmium erythraeum* (UniProt ID: Q10Z45), *Crocosphaera chwakensis* (A3IPT8), and *Thermus thermophilus* (UniProt ID: Q5SHV2). In contrast, *Synechocystis* PCC 6803 has two FutA homologies, denoted as FutA1 (UniProt ID: P72827) and FutA2 (UniProt ID: Q55835).

The sequences of the FutA homologues were aligned with Clustal Omega (26) and visualized with JalView (27), as shown in **Fig. S5**. Conservation of the physico-chemical properties of the amino acids across the sequence alignment is shown as a gradient from blue (low conservation) to yellow (high conservation) (27). The N-terminal signal peptide of *Prochlorococcus* MED4 (amino acids 1-27) as predicted by *SignalP* (1) (see *Molecular biology*, *Extended Materials and Methods*) was excluded from the alignment.

For species encoding a single FutA protein the arginine residue equivalent to Arg203 in *Prochlorococcus* MED4 FutA was conserved. Interestingly, this amino acid is even conserved *Synechocystis* PCC 6803 which has two FutA homologues, which may suggest that FutA1 and FutA2 both have capacity to bind Fe(III) or Fe(II) iron. This observation aligns with gene knockout studies conducted by us (28) demonstrating a degree of redundancy between the two FutA homologues.

The iron binding site in FpbA from *T. thermophilus* differs from the other proteins, as the residues equivalent to *Prochlorococcus* MED4 FutA His12 and Tyr13 are exchanged to Glycine and Glutamine, respectively. Despite this, the residue equivalent to Arg203 is conserved (Arg223). As FbpA switches from an open (PDB: 3WAE) to a closed conformation (PDB: 4ELR) upon iron binding, a carbonate ion is lost from the binding site and Arg223 is repositioned away from the binding site, **Fig. S4** (29, 30). This ability of Arg223 to act as a structural switch and maintain a net neutral charge in the binding site is therefore highly similar to the observed structural rearrangement of Arg203 in *Prochlorococcus* MED4 FutA.

Table S1. Data collection and refinement statistics for FutA structures reported (space group $P2_1$)

	Home Source	Neutron	SFX	SSX 5 kGy	SFX 350kGy
Temperature (°C)	21	21	25	21	25
Wavelength	1.54	3.10	1.13	0.97	1.13
# Integrated Lattices			78,743	5,278	24,378
# Merged Lattices			77,936	5,170	24,141
Unit Cell (a, b, c; Å)	39.4, 78.0, 48.0	39.5, 78.3, 47.9	39.1, 78.3, 47.4	39.7, 78.7, 48.4	39.4, 78.2, 48.0
β angle (°)	98.2	97.4	97.4	97.8	97.9
Resolution (all, Å)	47.50 – 1.70	24.95 – 2.1	30.10 – 1.60	40.97 – 1.76	32.42 – 1.65
Resolution (HR, Å)	1.73 – 1.70	2.18 – 2.1	1.63 – 1.60	1.79 – 1.76	1.68 – 1.65
R_{pim}[1,2] / R_{split}[1,3]	0.009 (0.089)[2]	0.106 (0.334)[2]	0.053 (0.089)[3]	0.235 (0.684)[3]	0.134 (0.691)[3]
CC ½ (%)[1]	100.0 (98.6)	97.1 (71.6)	99.6 (90.6)	92.3 (43.1)	97.0 (40.0)
$I/\sigma I$[1]	71.7 (11.6)	4.6 (1.9)	12.1 (4.6)	3.14 (0.41)	3.67 (0.43)
Completeness (%)[1]	97.9 (83.5)	80.8 (52.4)	99.8 (100.0)	100.0 (100.0)	100.0 (100.0)
Multiplicity[1]	65.4 (42.1)	1.3 (1.0)	618.7 (274.5)	26.2 (19.1)	165.2 (82.4)
Unique Reflections[1]	30,881 (1,369)	13,758 (886)	37,266 (1,877)	29,256 (1,467)	34,653 (1,676)
Wilson B-factor (Å^2)	14.10	9.85	12.09	24.28	21.24
	Home Source yellow	**Neutron blue**	**SFX green**	**SSX 5 kGy purple**	**SFX 350 kGy green**
PDB Code	8OEM	8RK1	8C4Y	8OGG	8OEI
Resolution (Å)	47.50 – 1.70	24.95 – 2.1	30.10 – 1.60	40.97 – 1.76	32.42 – 1.65
Rwork/Rfree	0.153 / 0.180	0.178 / 0.243	0.190 / 0.208	0.202 / 0.241	0.160 / 0.189
# Reflections all/free	30,847 / 1,588	13,748 / 698	37,266 /1,919	29,256 / 1,503	34,653 / 1,786
Number of Atoms					
Protein	2,558	2,492	2,485	2,509	2,572
Ion	1	1	1	1	1
Water	117	109	86	81	107
Clashscore (all)[4]	2.31	4.36	1.79	1.58	2.32
Ramachandran					
Preferred[4]	304	305	304	301	303
Allowed[4]	5	4	5	8	6
Outliers[4]	1	1	1	1	1
Z-score[2]	0.20±0.40	-1.70±0.40	0.07±0.41	-0.69±0.41	0.09±0.41
B-factors (Å^2)					
Protein	19.71	20.77	17.88	33.14	27.08
Water	25.32	41.10	23.32	33.65	33.04
R.M.S Deviations					
Bond Lengths (Å)	0.013	0.028	0.013	0.006	0.007
Bad bonds[4]	1 / 2,612	0 / 2,538	1 / 2,530	0 / 2,557	0 / 2,625
Bond Angles (°)	1.88	1.41	1.76	1.41	1.57
Bad angles[4]	8 / 3,537	1 / 3,427	5 / 3,416	1 / 3,456	2 / 3,553
Molprobity score[4]	1.01	1.21	0.94	1.02	1.07

[1]High resolution statistics in parentheses; [2]reports R_{pim}; [3]reports R_{split}; [4]determined by MolProbity (31)

Table S2. Bond lengths for the Fe coordination cage in the SFX and NMX structures following different refinement strategies as indicated in the text. All tabulated bond lengths are in Å.

	no link	Fe-Tyr link (restraint target 1.8 Å)				Fe-Tyr link (restraint target 2.004 Å)			
SFX 8C4Y									
Fe-O		0.01 σ	0.02 σ	0.03 σ	0.04 σ	0.01 σ	0.02 σ	0.03 σ	0.04 σ
Fe-Tyr13	1.82	1.80	1.80	1.80	1.80	1.94	1.86	1.83	1.82
Fe-Tyr143	1.96	1.87	1.93	1.95	1.96	1.99	1.98	1.98	1.98
Fe-Tyr199	1.89	1.83	1.85	1.86	1.87	1.95	1.91	1.89	1.89
Fe-Tyr200	1.83	1.81	1.82	1.82	1.82	1.93	1.87	1.84	1.83
Fe-Water	2.18	2.16	2.16	2.16	2.16	2.16	2.16	2.16	2.16
Average	1.94	1.89	1.91	1.92	1.92	1.99	1.96	1.94	1.94
NMX 8RK1									
Fe-Tyr13	2.19	1.82	1.88	1.94	1.99	2.01	2.04	2.06	2.09
Fe-Tyr143	1.95	1.81	1.85	1.89	1.92	2.01	2.01	2.01	2.01
Fe-Tyr199	2.01	1.81	1.84	1.86	1.89	2.00	2.00	2.01	2.01
Fe-Tyr200	1.93	1.81	1.85	1.88	1.90	2.00	2.00	1.99	1.98
Fe-Water	2.37	2.42	2.42	2.42	2.42	2.37	2.37	2.38	2.38
Average	2.09	1.93	1.97	2.00	2.02	2.08	2.08	2.09	2.09

Table S3. Full data collection and refinement statistics for two SSX dose series reported in space group $P2_1$ Data collection was carried out at 21 °C at an X-ray Energy of 12.8 keV for 10 consecutive exposures to give dose points at 5 kGy interval.

Data collection statistics for the 5 kGy SSX dose-series

Data Collection	**5 kGy**	**10 kGy**	**15 kGy**	**20 kGy**	**25 kGy**
Number of Integrated Lattices	5,278	5,089	5,197	5,158	5,227
Number of Merged Lattices	5,170	4,984	4,916	4,946	4,999
Unit Cell a, b, c (Å)	39.7, 78.7, 48.4	39.7, 78.7, 48.4	39.7, 78.7, 48.4	39.7, 78.7, 48.4	39.7, 78.7, 48.4
β (°)	97.8	97.8	97.8	97.8	97.8
Resolution, overall (Å)	40.97 – 1.76	40.97 – 1.76	40.97 – 1.76	40.97 – 1.76	40.97 – 1.76
Resolution, high (Å)	1.79 – 1.76	1.79 – 1.76	1.79 – 1.76	1.79 – 1.76	1.79 – 1.76
R_{split}[1]	23.5 (68.4)	25.1 (70.8)	20.6 (95.8)	24.9 (71.8)	24.3 (72.8)
CC ½ (%)[1]	92.3 (43.1)	91.0 (38.5)	91.0 (38.9)	89.8 (41.4)	90.7 (42.5)
$I/\sigma I$[1]	3.14 (0.41)	3.24 (0.41)	3.29 (0.42)	3.33 (0.41)	3.39 (0.40)
Completeness (%)[1]	100.0 (100.0)	100.0 (100.0)	100.0 (100.0)	100.0 (100.0)	100.0 (100.0)
Multiplicity[1]	26.2 (19.1)	25.8 (18.8)	25.7 (18.8)	25.5 (18.6)	26.1 (19.0)
Unique Reflections[1]	29,256 (1,467)	29,256 (1,469)	29,257 (1472)	29,258 (1471)	29,258 (1476)
Wilson B-factor ($Å^2$)	24.28	24.73	24.93	25.17	25.52

Data Collection	**30 kGy**	**35 kGy**	**40 kGy**	**45 kGy**	**50 kGy**
Number of Integrated Lattices	5,372	5,397	5,410	5,444	5,400
Number of Merged Lattices	5,119	5,110	5,115	5,160	5,147
Unit Cell a, b, c (Å)	39.7, 78.7, 48.4	39.7, 78.7, 48.4	39.7, 78.7, 48.4	39.7, 78.7, 48.4	39.7, 78.8, 48.4
β (°)	97.8	97.8	97.8	97.8	97.7
Resolution, overall (Å)	40.97 – 1.76	40.97 – 1.76	40.97 – 1.76	40.97 – 1.76	40.97 – 1.76
Resolution, high (Å)	1.79 – 1.76	1.79 – 1.76	1.79 – 1.76	1.79 – 1.76	1.79 – 1.76
R_{split}[1]	24.5 (76.4)	24.2 (75.4)	24.1 (74.9)	23.6 (78.3)	23.5 (79.1)
CC ½ (%)[1]	91.3 (37.2)	90.9 (31.1)	91.5 (38.7)	92.0 (34.9)	91.4 (32.8)
$I/\sigma I$[1]	3.24 (0.37)	3.26 (0.39)	3.31 (0.37)	3.24 (0.36)	3.18 (0.35)
Completeness (%)[1]	100.0 (100.0)	100.0 (100.0)	100.0 (100.0)	100.0 (100.0)	100.0 (100.0)
Multiplicity[1]	26.6 (19.4)	26.9 (19.6)	26.5 (19.4)	26.8 (19.7)	26.8 (19.6)
Unique Reflections[1]	29,263 (1,475)	29,265 (1,471)	29,266 (1,476)	29,270 (1,476)	29,273 (1,479)
Wilson B-factor ($Å^2$)	26.00	26.21	26.67	27.12	27.52

[1]High resolution statistics in parentheses

Table S4. Full data collection and refinement statistics for two SSX dose series reported in space group $P2_1$ (next pages). Data collection was carried out at 21 °C at an X-ray Energy of 12.8 keV for 10 consecutive exposures to give dose points at 22 kGy interval.

Data collection statistics for the 22 kGy SSX dose-series

Data Collection	**22 kGy**	**44 kGy**	**66 kGy**	**88 kGy**	**110 kGy**
Number of Integrated Lattices	9,015	9,760	10,114	9,914	9,533
Number of Merged Lattices	8,989	9,723	10,079	9,878	9,506
Unit Cell a, b, c (Å)	39.5, 78.2, 48.1	39.4, 78.2, 48.1	39.4, 78.3, 48.0	39.4, 78.3, 48.0	39.4, 78.3, 48.0
β (°)	97.8	97.8	97.7	97.7	97.7
Resolution, overall (Å)	40.71 – 2.10	40.71 – 2.10	40.71 – 2.10	40.71 – 2.10	40.72 – 2.10
Resolution, high (Å)	2.14 – 2.10	2.14 – 2.10	2.14 – 2.10	2.14 – 2.10	2.14 – 2.10
R_{split}[1]	20.5 (24.7)	18.5 (20.2)	16.9 (19.9)	16.3 (20.9)	16.6 (24.9)
CC ½ (%)[1]	91.9 (83.8)	93.1 (89.2)	94.4 (89.5)	94.8 (90.4)	94.8 (87.2)
$I/\sigma I$[1]	9.47 (3.04)	9.70 (2.88)	9.14 (2.35)	8.28 (1.87)	7.34 (1.46)
Completeness (%)[1]	100.0 (100.0)	100.0 (100.0)	100.0 (100.0)	100.0 (100.0)	100.0 (100.0)
Multiplicity[1]	43.2 (29.7)	51.2 (35.5)	57.8 (39.9)	58.8 (39.0)	56.5 (35.0)
Unique Reflections[1]	16,961 (855)	16,959 (863)	16,966 (866)	16,966 (865)	16,971 (861)
Wilson B-factor ($Å^2$)	18.52	20.31	22.63	24.80	26.59

Data Collection	**132 kGy**	**154 kGy**	**186 kGy**	**208 kGy**	**220 kGy**
Number of Integrated Lattices	8,546	7,476	6,825	6,297	5,738
Number of Merged Lattices	8,512	7,442	6,796	6,255	5,699
Unit Cell a, b, c (Å)	39.4, 78.4, 48.1	39.4, 78.4, 48.1	39.4, 78.4, 48.1	39.4, 78.3, 48.1	39.4, 78.3, 48.1
β (°)	97.7	97.7	97.7	97.7	97.7
Resolution, overall (Å)	40.70 – 2.10	40.71 – 2.10	40.72 – 2.10	40.72 – 2.10	40.73 – 2.10
Resolution, high (Å)	2.14 – 2.10	2.14 – 2.10	2.14 – 2.10	2.14 – 2.10	2.14 – 2.10
R_{split}[1]	16.8 (28.7)	17.7 (39.5)	18.4 (51.2)	18.5 (61.8)	19.6 (76.9)
CC ½ (%)[1]	95.3 (84.3)	94.9 (75.0)	94.5 (63.6)	95.6 (58.4)	95.6 (47.1)
$I/\sigma I$[1]	6.28 (1.15)	5.19 (0.92)	4.23 (0.77)	3.43 (0.70)	2.88 (0.63)
Completeness (%)[1]	100.0 (100.0)	100.0 (100.0)	100.0 (100.0)	100.0 (100.0)	100.0 (100.0)
Multiplicity[1]	50.6 (28.0)	44.9 (20.8)	41.4 (15.5)	38.1 (10.9)	34.3 (8.2)
Unique Reflections[1]	16,977 (862)	16,981 (860)	16,983 (856)	16,986 (859)	16,989 (861)
Wilson B-factor ($Å^2$)	27.84	29.60	30.88	31.55	37.88

[1]High resolution statistics in parentheses

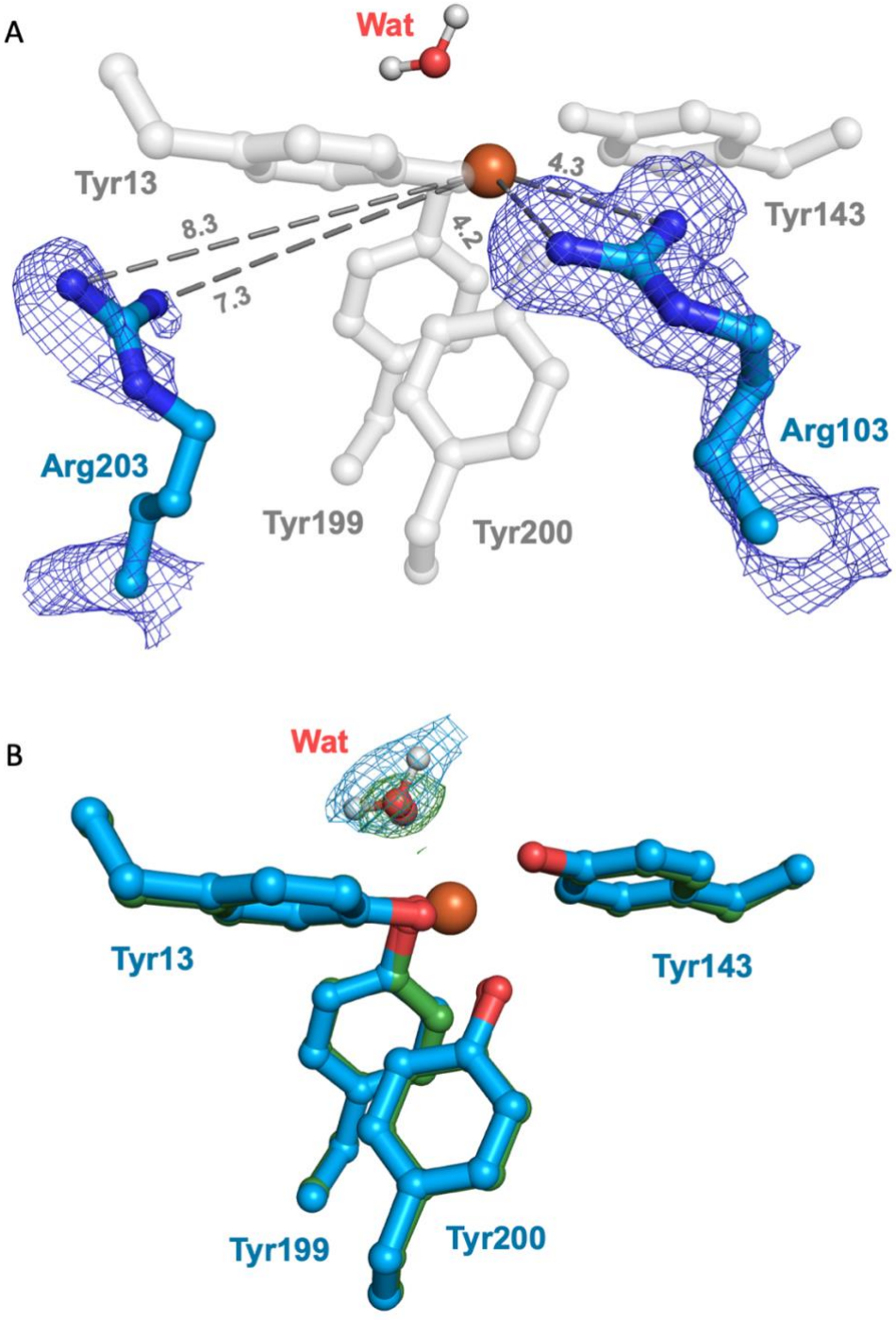

Figure S1. The iron center of FutA (Fe(III) state) by neutron diffraction. (*A*), the nuclear density ($2F_{obs} - F_{calc}$, blue, contoured at 1.5σ) reveals positioning of the side chain of Arg103 close to the tyrosinates, while the Arg203 side chain does not engage in interactions (similar to the SFX structure **Fig. 2D**). (*B*), comparison of the nuclear density ($2F_{obs} - F_{calc}$, blue, contoured at 1.5σ) with the electron density of the SFX structure ($2F_{obs} - F_{calc}$, green, contoured at 1.5σ). Dashed lines show distances in Å. Carbons shown blue for NMX and green for SFX, heteroatoms colored as in **Fig. 1**.

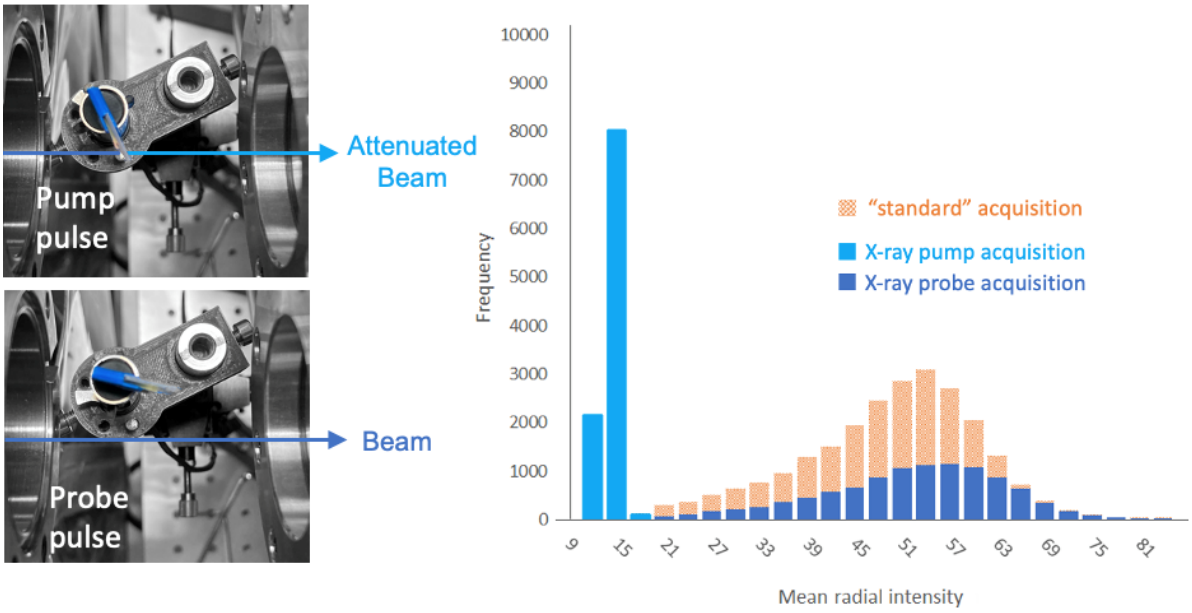

Figure S2: Overview of the experimental setup and data analysis for the XFEL X-ray pump probe experiment. A fast, self-restoring rotary shutter (Branstrom Instruments, USA) mounted upstream of the sample and containing a sapphire wafer in a range of thicknesses was placed in the path of the XFEL beam. This flipper-attenuator was TTL triggered from a signal generator to move the wafer and reduce the flux with alternating pulses, while two diffraction images corresponding to X-ray pump and X-ray probe were collected on the same crystal with the fixed target stationary (left), before the fixed target chip was advanced to the next position. Pump and probe images were separated based on average diffraction intensity (diffraction spots and background) as calculated for each diffraction image and plotted as a histogram against frequency (right). The X-ray pump (light blue) is distinguished from the X-ray probe (dark blue) by its lower average diffraction intensity. For comparison, a histogram for a standard SFX experiment is shown (salmon).

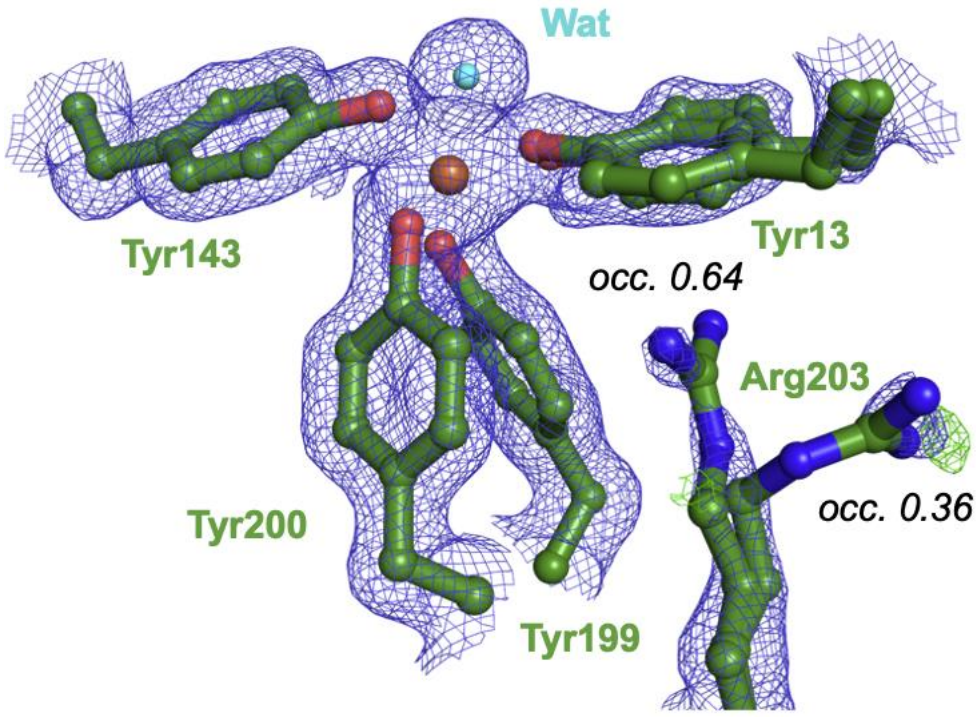

Figure S3. Refined SFX X-ray probe structure **Fig. 4**. The side chain of Arg203 was refined in dual occupancy, as indicated. Density shown in blue is 2Fo-Fc at 1 σ, difference density Fo-Fc, shown in green, 3 σ; no negative difference density was observed. Heteroatoms colored as in **Fig. 1**.

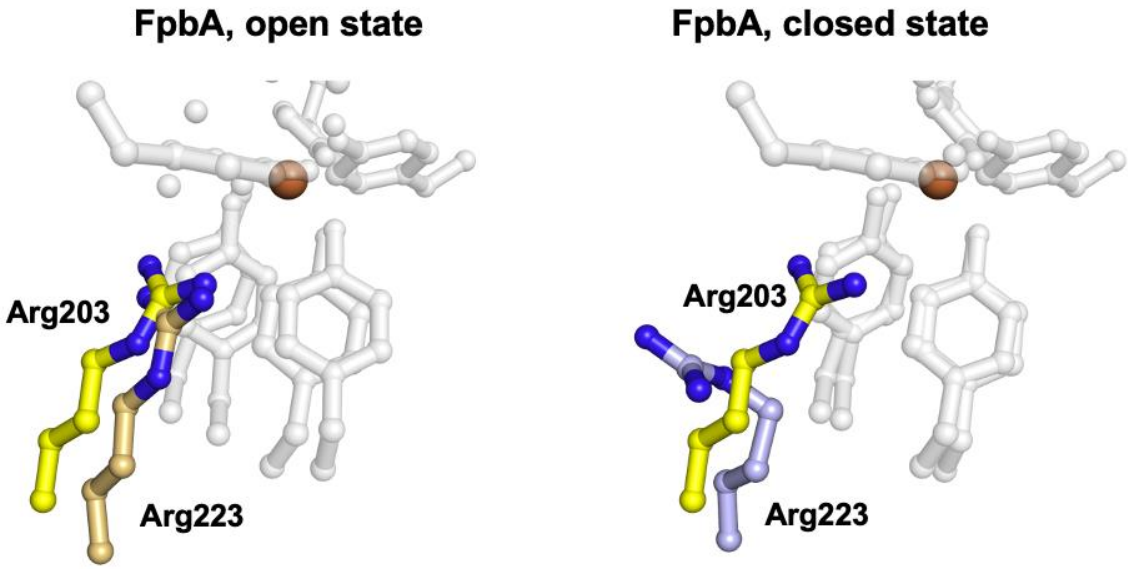

Figure S4: Overlay of Fe(II) bound *Prochlorococcus* MED4 FutA (yellow) with *Thermus thermophilus* FbpA in the open (light orange, PDB:3WAE) and closed conformations (light purple, PDB:4ELR). As FpbA switches from an open to a closed conformation, a carbonate ion is lost and Arg233 is repositioned to maintain a net neutral charge in the binding site. The repositioning of Arg233 in FbpA is highly similar to the structural switch of Arg203 in FutA.

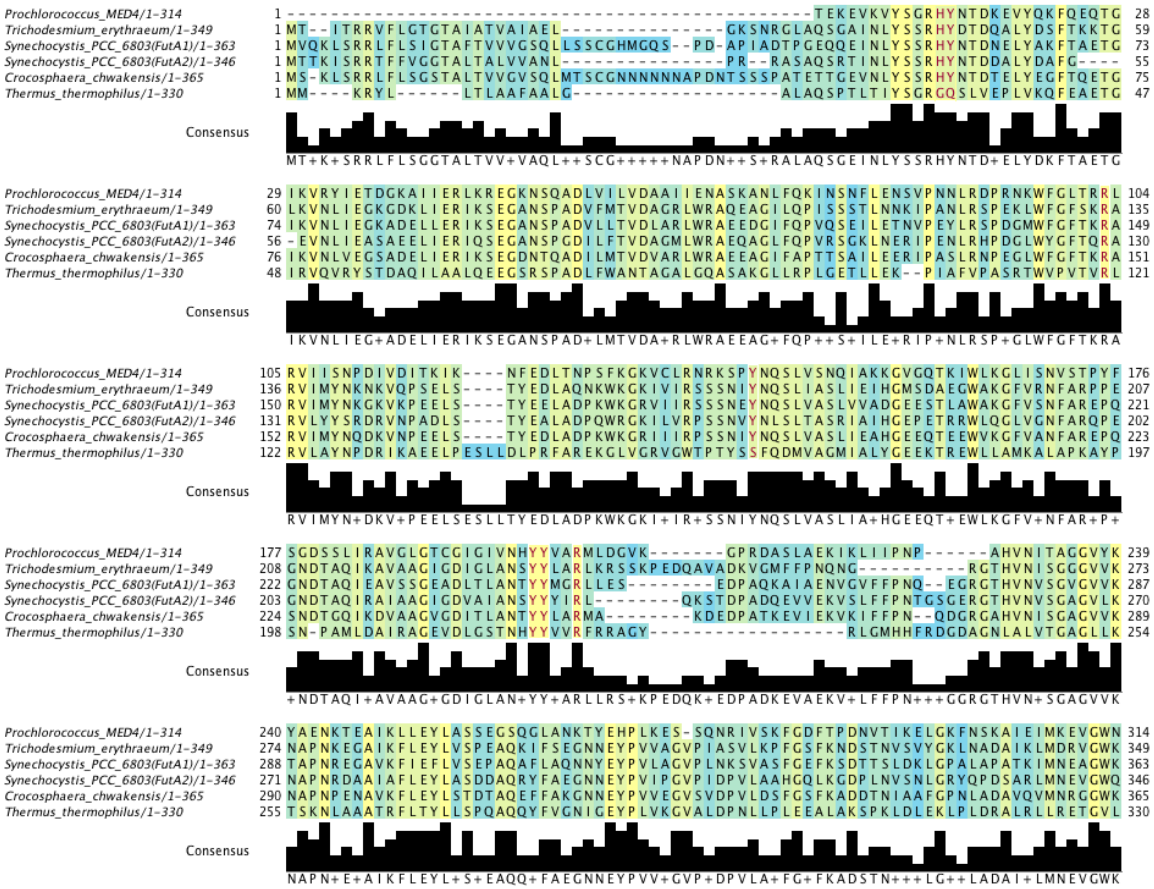

Figure S5: Multiple sequence alignment of the FutA homologues from *Prochlorococcus* MED4 (UniProt ID: Q7V0T9, excluding signal peptide amino acids 1-27), *Trichodesmium erythraeum* (UniProt ID: Q10Z45), *Synechocystis* PCC 6803 (FutA1 UniProt ID: P72827 and FutA2 UniProt ID: Q55835), *Crocosphaera chwakensis* (A3IPT8), and *Thermus thermophilus* (UniProt ID: Q5SHV2) carried out with Clustal Omega (26) and Jalview (27). Iron coordinating amino acids in Prochlorococcus MED4 are shown in red. The consensus graph indicates the number of times the modal residue appears at each position, while "+" denotes positions where the modal residue is shared by more than one amino acid. The blue and yellow gradient shading indicates the degree of conservation of the physio-chemical properties of the amino acids at each position, where blue indicates low conservation and yellow indicates high conservation.

References

1. J. J. Almagro Armenteros *et al.*, SignalP 5.0 improves signal peptide predictions using deep neural networks. *Nature Biotechnology* **37**, 420-423 (2019).
2. J. H. Beale *et al.*, Successful sample preparation for serial crystallography experiments. *Journal of Applied Crystallography* **52**, 1385-1396 (2019).
3. S. Horrell *et al.*, Fixed Target Serial Data Collection at Diamond Light Source. *J Vis Exp* 10.3791/62200 (2021).
4. W. Kabsch, XDS. *Acta Crystallographica Section D* **66**, 125-132 (2010).

5. P. R. Evans, G. N. Murshudov, How good are my data and what is the resolution? *Acta Crystallographica Section D* **69**, 1204-1214 (2013).
6. Z. Otwinowski, W. Minor, Processing of X-ray diffraction data collected in oscillation mode. *Methods in Enzymology* **276**, 307-326 (1997).
7. G. Winter *et al.*, DIALS: implementation and evaluation of a new integration package. *Acta Crystallographica Section D* **74**, 85-97 (2018).
8. M. Uervirojnangkoorn *et al.*, Enabling X-ray free electron laser crystallography for challenging biological systems from a limited number of crystals. *Elife* **4** (2015).
9. P. Howell, G. Smith, Identification of heavy-atom derivatives by normal probability methods. *Journal of applied crystallography* **25**, 81-86 (1992).
10. T. Nakane *et al.*, Data processing pipeline for serial femtosecond crystallography at SACLA. *Journal of Applied Crystallography* **49**, 1035-1041 (2016).
11. J. Hattne *et al.*, Accurate macromolecular structures using minimal measurements from X-ray free-electron lasers. *Nature Methods* **11**, 545-548 (2014).
12. A. Vagin, A. Teplyakov, MOLREP: an Automated Program for Molecular Replacement. *Journal of Applied Crystallography* **30**, 1022-1025 (1997).
13. P. Emsley, B. Lohkamp, W. G. Scott, K. Cowtan, Features and development of Coot. *Acta Crystallogr D Biol Crystallogr* **66**, 486-501 (2010).
14. L. Catapano *et al.*, Neutron crystallographic refinement with REFMAC5 from the CCP4 suite. *Acta Crystallogr D Struct Biol* **79**, 1056-1070 (2023).
15. G. N. Murshudov *et al.*, REFMAC5 for the refinement of macromolecular crystal structures. *Acta Crystallogr D Biol Crystallogr* **67**, 355-367 (2011).
16. J. Sanchez-Weatherby *et al.*, Improving diffraction by humidity control: a novel device compatible with X-ray beamlines. *Acta Crystallogr D Biol Crystallogr* **65**, 1237-1246 (2009).
17. C. R. Harris *et al.*, Array programming with NumPy. *Nature* **585**, 357-362 (2020).
18. W. McKinney, Data Structures for Statistical Computing in Python. *Proceedings of the 9th Python in Science Conference* **445**, 56-61 (2010).
19. P. Virtanen *et al.*, SciPy 1.0: fundamental algorithms for scientific computing in Python. *Nature Methods* **17**, 261-272 (2020).
20. J. D. Hunter, Matplotlib: A 2D Graphics Environment. *Computing in Science & Engineering* **9**, 90-95 (2007).
21. S. Grazulis *et al.*, Crystallography Open Database (COD): an open-access collection of crystal structures and platform for world-wide collaboration. *Nucleic Acids Res.* **40**, D420-427 (2012).
22. M. Gurusaran, M. Shankar, R. Nagarajan, J. R. Helliwell, K. Sekar, Do we see what we should see? Describing non-covalent interactions in protein structures including precision. *IUCrJ* **1**, 74-81 (2014).
23. C. S. Bury, J. C. Brooks-Bartlett, S. P. Walsh, E. F. Garman, Estimate your dose: RADDOSE-3D. *Protein Science* **27**, 217-228 (2018).
24. J. L. Dickerson, P. T. N. McCubbin, E. F. Garman, RADDOSE-XFEL: femtosecond time-resolved dose estimates for macromolecular X-ray free-electron laser experiments. *J. Appl. Cryst.* **53**, 549-560 (2020).
25. J. L. Dickerson, E. F. Garman, Doses for experiments with microbeams and microcrystals: Monte Carlo simulations in RADDOSE-3D. *Protein Sci* **30**, 8-19 (2021).
26. F. Sievers *et al.*, Fast, scalable generation of high-quality protein multiple sequence alignments using Clustal Omega. *Molecular Systems Biology* **7**, 539 (2011).
27. A. M. Waterhouse, J. B. Procter, D. M. A. Martin, M. Clamp, G. J. Barton, Jalview Version 2—a multiple sequence alignment editor and analysis workbench. *Bioinformatics* **25**, 1189-1191 (2009).
28. D. Polyviou *et al.*, Structural and functional characterization of IdiA/FutA (Tery_3377), an iron-binding protein from the ocean diazotroph Trichodesmium erythraeum. *Journal of Biological Chemistry* **293**, 18099-18109 (2018).
29. P. Lu *et al.*, Functional characterisation of two ferric-ion coordination modes of TtFbpA, the periplasmic subunit of an ABC-type iron transporter from Thermus thermophilus HB8. *Metallomics* **11**, 2078-2088 (2019).
30. S. Wang *et al.*, A novel mode of ferric ion coordination by the periplasmic ferric ion-binding subunit FbpA of an ABC-type iron transporter from Thermus thermophilus HB8. *Acta Crystallographica Section D* **70**, 196-202 (2014).
31. C. J. Williams *et al.*, MolProbity: More and better reference data for improved all-atom structure validation. *Protein Sci* **27**, 293-315 (2018).